Materials Advances

ROYAL SOCIETY OF CHEMISTRY

PAPER

View Article Online
View Journal | View Issue



Cite this: *Mater. Adv.*, 2025, 6, 9437

# PDGF-loaded eugenol-impregnated biocompatible nanofibrous scaffolds for enhanced diabetic wound healing and vascularization

Lakshimipriya Sethuram and Natarajan Chandrasekaran *

Diabetic foot ulcers (DFUs) represent a major clinical challenge due to their high infection risk, long-term severe infections and limb amputations. In the current study, multifunctional platelet-derived growth factor (PDGF)-impregnated eugenol microemulsion (EuME)-based silver nanocomposites (PDGF/EuME–AgNPs/CSNs) embedded within a PVA/chitosan base matrix have been fabricated. The synergistic effects of PVA/chitosan accelerate wound closure while exhibiting broad-spectrum antimicrobial and anti-inflammatory properties. The polymeric matrix facilitates proliferation and migration of keratinocytes and fibroblasts, promoting tissue regeneration. The electrospun nanofibrous mats exhibited homogenous surface morphology with a uniform pore size distribution of 100–250 nm, a water uptake and absorption percentage of 96%, an optimal porosity of 94.7, a mass loss capacity of 60.36%, a water contact angle of 68° and a tensile strength of 1.2 MPa, facilitating mechanical flexibility and providing an optimal moist wound environment. The PDGF/EuME–AgNPs/CSNs scaffolds demonstrated 95% antimicrobial inhibitory activity against *S. aureus* and *P. aeruginosa*. *In vivo* studies showed significantly accelerated wound contraction by the 9th day, achieving maintenance of 98% glycemic levels when compared to control groups, which exhibited 20% wound contraction ($p < 0.01$). The nanofibers reduce inflammation and promote fibroblast production, collagen deposition, and fibrin regeneration. Increased levels of CD-31, IL-1, and TGF-β confirmed improved re-epithelialization, vascularization, and skin regeneration. The findings suggested that PDGF/EuME–AgNPs/CSNs accelerate diabetic wound healing, enable sustained growth factor delivery, and promote vascularization and re-epithelialization, demonstrating their potential in improving DFU treatment outcomes.

Received 4th April 2025,
Accepted 8th October 2025

DOI: 10.1039/d5ma00322a

rsc.li/materials-advances



## 1. Introduction

An impaired wound healing response is a devastating complication in diabetes mellitus (DM) patients, which is caused by the release of free radicals resulting in the destruction of cellular constituents, namely, proteins, lipids and DNA.[1] Diabetic wounds occur due to decreased vascular recovery, exhilarated apoptosis and abnormal inflammatory behavior, accompanied by prolonged hospitalization and limb amputations. Wound treatment is quite challenging, and the recurrence rate of diabetic wounds is high. In order to overcome the recurrence and exacerbation, the vascularization potential, skin re-epithelialization, biofilm inhibition, deposition of fibroblasts with collagen production, and proper supply of blood flow should be well addressed. Commercially available wound dressings, namely, hydrocolloids, foams, alginates and gauzes, cause severe periwound damage to the areas of the body prone to friction and infections and still exhibit many limitations.[2] Silver ion based wound dressing bandages procured from conventional platforms contain polyamides and silver sulfadiazine, which help in efficient antimicrobial activity and control wound exudate at the site of injury. Although silver bandages protect the wound site from bacterial infections and aid in both acute and chronic wound healing applications, the toxicity response to simulated human wound fluids is dominant and a quantitative amount of silver ions released into the biological environment is instant and connected with *in vitro* toxicity.[3]

Eugenol, a volatile phenolic monoterpene generated from the guaiacol component, is typically found in nutmeg, cinnamon, pepper, and clove. It is a rich source of flavonoids that enhance the rate of epithelialization, modulate inflammatory cytokines, and promote vascularization in chronic wounds.[4] The combined effect of PVA/chitosan facilitates diabetic wound healing by rendering good biocompatibility, cellular bioactivity, cell and tissue penetration efficiency, mechanical stability and rigidity, an ideal moist environment for wound healing and

*Centre for Nanobiotechnology, Vellore Institute of Technology, Vellore, Tamil Nadu, India. E-mail: nchandrasekaran@vit.ac.in; Fax: +91 416 2243092; Tel: +91 416 2204212*

efficient water uptake and exhibits excellent anti-microbial and anti-inflammatory properties. The wound dressings made up of PVA/chitosan as a base polymeric matrix enhance fibroblast and collagen differentiation and migration, and reduce inflammation and reactive oxygen species, resulting in accelerated wound closure and contraction.[5] Platelet derived growth factor (PDGF) is a potent dimeric glycoprotein that stimulates proliferation, vascularization, and skin and tissue repair applications. Intracellular administration of PDGF into nanomaterials augments the influx of fibroblasts and collagen formation, which could accelerate extracellular matrix restoration and enhance wound healing.[6] In the case of diabetic wounds, PDGF promotes macrophage activity, attracts fibroblasts and collagen into the wound space, and increases neovascularization and epithelialization at the chronic wound site.[7] The impregnation of drug/bioactive molecules into thin nanofibrous structures remains challenging, and the nature of scaffold properties should not be adversely affected. Hence, in drug delivery paradigms, a defined core–sheath design using co-axial electrospinning is essential to impregnate active agents or drugs into the core part of the nanomaterial in order to avoid disruption/damage to the drugs.[8]

In this study, we fabricated a core–sheath structured PDGF based eugenol impregnated nanofibrous mat for the modulation of inflammation, proliferation, skin remodelling and vascularization potential in diabetic wounds (Fig. 1). Upon application to the wound, the PDGF/EuME–AgNPs/CSNs effectively disrupt the formation of bacterial biofilms, and the embedded eugenol microemulsion eradicates the underlying bacteria, which were hardly affectedby the antimicrobial drugs. Eugenol – an allyl chain-substituted guaiacol extracted from clove possessing excellent anti-inflammatory and antioxidant properties – present within the core part of the nanofibrous mat releases phenolic compounds in a sustained manner. Engrailed-1 (En1) is a gene that plays a crucial role in collagen and fibroblast deposition during wound healing; however, excessive collagen deposition is not recommended as it may result in thickened scar formation during the healing process. In order to reduce this thickened scar formation, the released eugenol inhibits En1, preventing the overproduction of scar tissue and promoting an efficient skin regeneration cycle.[9] Meanwhile, the exposed core PDGF initiated the regulation of the immune microenvironment by adhering to and neutralizing inflammatory factors to induce polarization of macrophages from M1 to M2 phenotype, fostering the phase transition from inflammation to remodeling.[10] In this design, effective vascularization, faster wound healing, restoration of native extracellular matrix (nECM), accelerated fibroblast and collagen deposition and scarless wound healing were achieved in treating diabetic wound infections in streptozotocin induced Wistar albino rat models.

# 2. Experimental section

## 2.1. Materials

Eugenol (an aromatic essential oil), Tween 80 (surfactant), chitosan (degree of deacetylation $\geq$ 75.00%), polyvinyl alcohol (PVA) ($M_W$ 89 000–98 000, 99% hydrolyzed), nutrient broth (NB), nutrient agar (NA), Muller-Hinton broth (MHB), Muller-Hinton agar (MHA), streptozotocin (STZ) (*N*-(methylnitrosocarbamoyl)-α-D-glucosamine $\geq$ 98.00%), citric acid ($C_6H_8O_7$), sodium citrate tribasic dihydrate and acetic acid ($CH_3COOH$, 99.7%) were procured from HiMedia Laboratories, LBS Marg, Mumbai, India. Silver nitrate ($AgNO_3$) (ACS reagent, Z99.0%), platelet derived growth factor (PDGF-BB, recombinant, expressed in *E. coli*), potassium chloride, sodium chloride, calcium chloride, bovine serum albumin and sodium bicarbonate were obtained from Sigma-Aldrich. *S. aureus* (ATCC 6538P™) and *P. aeruginosa* (ATCC 27853™) were obtained from Microbiologics, USA. Ethanol-D was obtained from Gladwin, Poland.

## 2.2. Optimization and formulation of colloidal nanomaterials

The oil-in-water (O/W) microemulsion was prepared by varying the oil : surfactant ratio using a magnetic stirrer by standardizing the temperature at 37 °C and stirring at 400 rpm for 10 minutes.[11] The silver nanoparticles were formulated using a eugenol microemulsion (EuME–AgNPs). Briefly, 1 mM of $AgNO_3$ was added drop by drop to EuME (1%, 3%, 5%, 7% and 9%) by optimizing time and temperature at 1–40 hours and 37 °C, respectively, at 300 rpm.[12] Response surface methodology (RSM) was used as the experimental design in order to quantitatively optimize the synthesis parameters and assess their combined impact on nanoparticle properties. In order to identify the best conditions for minimizing particle size and polydispersity index while maximizing zeta potential and colloidal stability, RSM was used due to its effectiveness in modelling and analyzing multivariable systems. The mean hydrodynamic droplet/particle size, polydispersity index and zeta potential of the synthesized nanocolloids were determined. Also, in order to assess long-term kinetic stability, the prepared formulations (EuME & EuME–AgNPs) were stored in amber airtight glass containers ranging from −20 °C to 4 °C and analyzed at specific time intervals (0, 2, 4 and 6 months) using dynamic light scattering in order to observe the droplet/particle size and polydispersity index (pDI). In addition, the formulated EuME and EuME–AgNPs were monitored for any phase separation or particle aggregation.

## 2.3. Preparation of core–sheath nanofibers using co-axial electrospinning

Initially, 10% w/v PVA was dissolved in a 2% acetic acid solution ($CH_3COOH$) and stirred for a couple of hours at 90 °C. To a desired volume of PVA, different concentrations of EuME (1%, 3%, 7%, and 9%) and EuME–AgNPs (1%, 3%, 7%, and 9%) were added and blended, followed by agitation for 2 hours (700 rpm) at 37 °C. After the blending process, the EuME and EuME–AgNPs impregnated PVA solutions were maintained under static conditions for 24 hours at room temperature in order to prevent structural instability. In order to enhance fibroblast proliferation and intraepithelial collagen deposition in the chronic wound model, varying concentrations of PDGF (1%, 3%, 7%, and 9%) were impregnated with EuME–AgNPs and PVA solution and blended for 20 minutes (300 rpm)

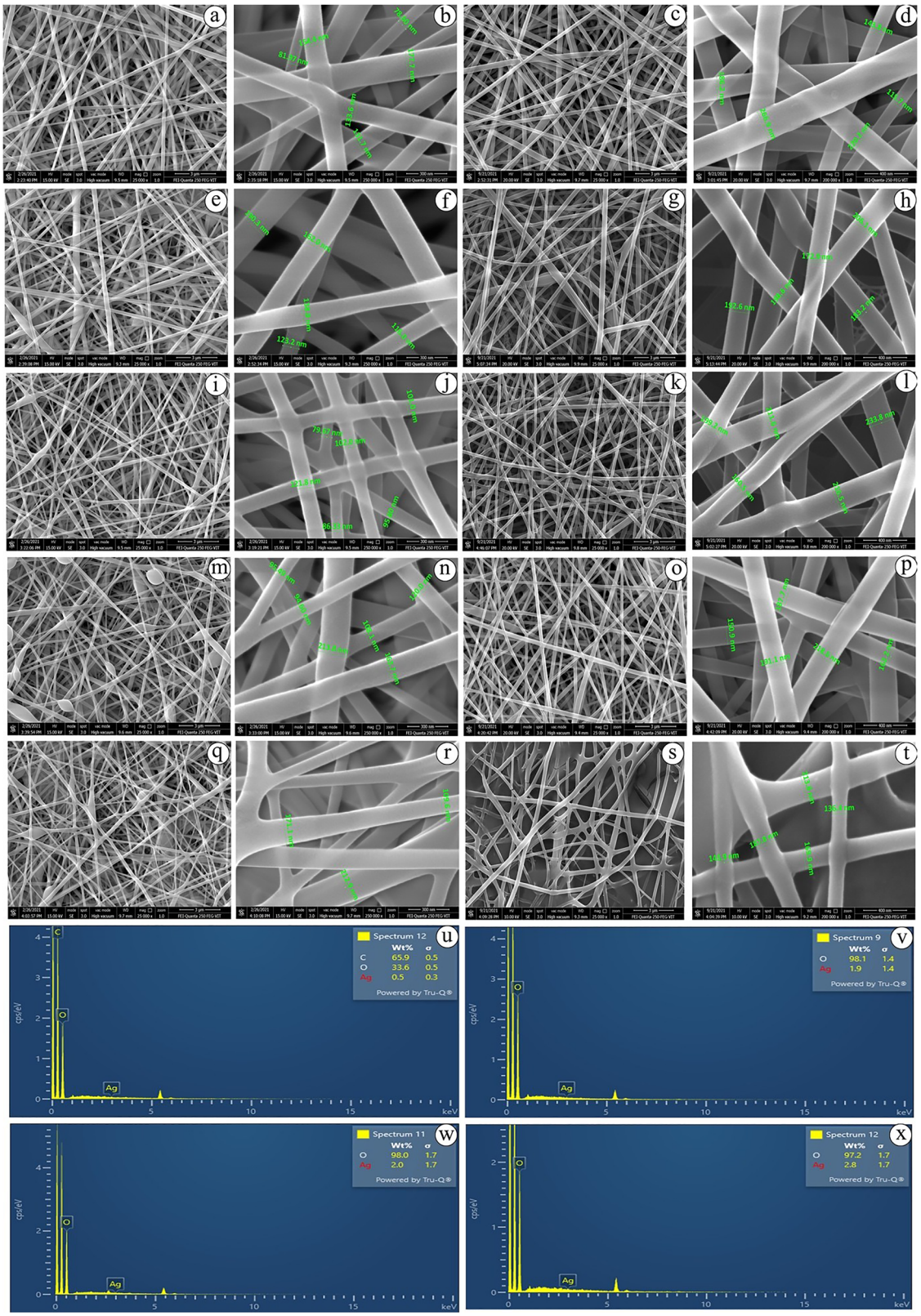


Fig. 1 Surface morphology (FESEM) (a–t) and elemental composition (EDAX) (u–x) of core–sheath nanofibrous mats (CSNs) (before and after the crosslinking process): (a and b) 10% PVA matrix before crosslinking, (c and d) 10% PVA matrix after crosslinking, (e and f) chitosan:PVA/CSNs before crosslinking, (g and h) chitosan:PVA/CSNs after crosslinking, (i and j) EuME/CSNs before crosslinking, (k and l) EuME/CSNs after crosslinking, (m and n) EuME–AgNPs/CSNs before crosslinking, (o and p) EuME–AgNPs/CSNs after crosslinking, (q and r) PDGF/EuME–AgNPs/CSNs before crosslinking, (s and t) PDGF/EuME–AgNPs/CSNs after crosslinking, (u and v) EuME–AgNPs/CSNs before and after crosslinking, and (w and x) PDGF/EuME–AgNPs/CSNs before and after crosslinking.

at room temperature. After impregnation of PDGF with EuME–AgNPs, the encapsulation efficiency (%) of PDGF was calculated as follows: the free (unencapsulated) PDGF added was subtracted from the total PDGF added divided by the total PDGF impregnated, giving the total encapsulation efficiency (%) of PDGF/EuME–AgNPs. Furthermore, the blended PDGF-impregnated eugenol microemulsion-based silver nanoparticles (PDGF/EuME–AgNPs) serve as the core layer solution in the co-axial electrospinning process for the fabrication of CSNs. Secondly, 3% (w/v) of deacetylated chitosan $(C_6H_{11}NO_4)n$ was dissolved in 2% acetic acid and agitated for 24–48 hours at 37 °C, and the resulting solution serves as the sheath layer solution in the co-axial electrospinning process for the fabrication of CSNs.

The blended solutions (PVA, chitosan:PVA, EuME, EuME–AgNPs, and PDGF-impregnated EuME–AgNPs) were prepared. The spinning parameters were optimized by varying the flow rate which ranges between 0.1–1 mL $h^{-1}$; the applied electric field which ranges between 15–30 kV; the tip–rotor interspace which ranges between 10–30 cm; the translation speed between ranges 65–70; and the drum speed which ranges between 500–800 rpm. The temperature and percentage of humidity were kept constant. Apart from the electrospinning parameters optimized for nanofabrication, the needle diameter, solvent selection, collector type and configuration, collector surface area, polymer solution mixing and homogenization were parallelly optimized to fabricate homogenous and bead-free nanofibrous mats. The fabricated CSNs were termed chitosan:PVA/CSNs, EuME/CSNs, EuME–AgNPs/CSNs, and PDGF/EuME–AgNPs/CSNs. The CSNs were kept under high vacuum conditions at 37 °C for 24 hours to maintain the structural integrity of the nanofibers. Post-fabrication, chemical crosslinking of nanofibers was performed using 50% glutaraldehyde in a sealed high vacuum desiccator for 2 hours at 37 °C. After 2 $\frac{1}{2}$ hours, the chemically crosslinked nanofibers were allowed to vaporize dry for 24 hours at 60 °C.

### 2.4. Microstructural characterization of nanofibers

The surface morphology of PVA, chitosan:PVA/CSNs, EuME/CSNs, EuME–AgNPs/CSNs, and PDGF/EuME–AgNPs/CSNs was analyzed at a voltage of 20 kV using a Quanta 250 FEG FESEM. The elemental composition of CSNs, namely EuME–AgNPs/CSNs and PDGF/EuME–AgNPs/CSNs, was determined using energy dispersive X-ray spectroscopy (EDAX) to calculate the quantitative amounts of chemical elements. The internal morphology of CSNs (EuME/CSNs, EuME–AgNPs/CSNs, and PDGF/EuME–AgNPs/CSNs) was examined using high-resolution transmission electron microscopy (HR-TEM) and selected area electron diffraction (SAED; JEM-2100 Plus, JEOL, Japan). The presence of functional groups in CSNs (PVA, chitosan:PVA/CSNs, EuME/CSNs, EuME–AgNPs/CSNs, and PDGF/EuME–AgNPs/CSNs) was analyzed using Fourier transform infrared spectroscopy (FTIR). FTIR measurements were conducted using a PerkinElmer Spectrum Instrument (Waltham, USA) at a resolution of 4 $cm^{-1}$. The crystalline nature of CSNs (PVA, chitosan:PVA/CSNs, EuME/CSNs, EuME–AgNPs/CSNs, and PDGF/EuME–AgNPs/CSNs) was investigated using X-ray powder diffraction (D8 Advance, Bruker, Germany) with a 2.2 kW Cu-anode ceramic tube source.

### 2.5. Mechanical and physico-chemical testing

A load cell rated at 2 N operating at a defined cross speed (10 mm $mm^{-1}$ $min^{-1}$) was used to analyze the tensile strength of nanofibers on an Instron 5567 uniaxial-tensile testing machine. The stress–strain curve models were used to determine the tensile strength (MPa) of CSNs. Each sample specimen ($n$ = 2) was obtained in triplicate.[13] The hydrophilicity of CSNs was assessed by measuring the water droplet contact angle (WDCA) at 37 °C using a sessile drop technique. After five seconds, the CSNs were positioned and scaled on the nanofiber surface with six independent point variables. The contact angle (°) was determined. The liquid displacement technique was used to measure the porosity of CSNs.[14] The nanofibers were placed in a known volume of ethanol ($V_1$) measured with a graduated cylinder for nearly 30 minutes. The volume of ethanol after incorporation into nanofibrous mats was recorded as $V_2$. After the incorporated nanofibrous mats were removed, the remaining volume of ethanol ($V_3$) was calculated. The porosity of nanofibers (%) was measured using eqn (1):

$$\text{Porosity (\%)} = ((V_1 - V_3)/(V_2 - V_3)) \times 100 \quad (1)$$

The water uptake of CSNs was determined by weighing each dry nanofibrous mat and immersing it in deionized water at room temperature for 1 hour.[15] The weight of each nanofibrous mat was calculated after removing excess water using filter paper. The percentage of water uptake (%) was measured using eqn (2):

$$\text{Water uptake (\%)} = ((W - W_i)/(W_i)) \times 100 \quad (2)$$

where $W_i$ corresponds to the initial weight of CSNs and $W$ corresponds to the final weight of CSNs (g) after immersing in deionized water for 1 hour. The percentage of water uptake was calculated from triplicate measurements. The mass loss of CSNs was measured in phosphate buffered saline (PBS) at 37 °C with pH 7.4 by mimicking the natural body environment.[16] Briefly, each CSN was uniformly soaked in PBS solution, followed by extraction at the required time points (1, 2, 3, 7, 14, 21, and 28 hours) and the residual water present on the specimen was removed using filter paper. The percentage of mass loss can be calculated using eqn (3):

$$\text{Mass loss (\%)} = ((W_i - W_{f)}/(W_i)) \times 100 \quad (3)$$

where $W_i$ and $W_f$ correspond to the initial and final masses of core–sheath nanofibers (g), respectively. The percentage of mass loss was determined from triplicate measurements.

### 2.6. Antimicrobial efficacy

The antimicrobial activity of chitosan:PVA, EuME, EuME–AgNPs, PDGF/EuME–AgNPs, and SBD–AgNPs was determined. The microbial strains used for antimicrobial activity were *S. aureus* and *P. aeruginosa*. Aliquots were proportionately mixed with bacterial cultures comprising $10^6$ to $10^7$ CFU. After growing the bacteria for 24 hours, the concentration of bacteria was determined to be

$1 \times 10^8$ CFU $mL^{-1}$ and serially diluted with MHB (0.1 OD). Different working concentrations of chitosan:PVA, EuME, EuME–AgNPs, PDGF/EuME–AgNPs, and SBD–AgNPs were interacted with the appropriate bacterial cultures. After 24 hours of incubation at 37 °C, MHB and gentamicin were utilized as the negative and positive controls, respectively. In order to observe the color change, 10 μL of resazurin dye suspension was further added to each well.[8] Using the well diffusion process, the antibacterial activity of chitosan:PVA, EuME, EuME–AgNPs, PDGF/EuME–AgNPs, and SBD–AgNPs was assessed. Diffusion wells were punched and uniformly swabbed with bacterial cultures. Solutions of chitosan:PVA, EuME, EuME–AgNPs, PDGF/EuME–AgNPs, and SBD–AgNPs were introduced to diffusion wells at various concentrations, and samples were allowed to diffuse. Gentamicin (an antibiotic) solution was introduced in an equal ratio to the control well. After diffusion, the agar plates were allowed to incubate at 37 °C for 18 hours. Furthermore, the plates were examined to visually measure the zone of inhibition against *S. aureus* and *P. aeruginosa*. Under exposure to light, a transparent ruler or caliper was used to measure the zone of inhibition in the Petri dish from one end to the other end of the clear zone. The zone of inhibition was measured in millimetres against *S. aureus* and *P. aeruginosa*.

### 2.7. Hemocompatibility studies

**2.7.1. Percentage of cell viability (WBCs).** To extract the pure white buffy coats, human white blood cells were extracted and combined with Ficoll hypaque gradient (FHG).[17,18] The isolated lymphocytes were subcultured in 50% Roswell Park Memorial Institute-1640 (RPMI) medium with 10% fetal calf serum (FCS) and allowed to reach a predetermined density of $10^6$ cells per mL. They were then added in 2 mM of L-glutamine and streptomycin and maintained at 37 °C with 5% $CO_2$. The interaction of the freshly isolated lymphocytes took place within 24 hours, which is referred to as time 0 ($T^0$). Each individual flask was filled with $15 \times 10^6$ lymphocytes and treated with eugenol-based nanomaterials, namely chitosan:PVA, EuME, EuME–AgNPs, PDGF/EuME–AgNPs and SBD–AgNPs, *via* culture media. Cell viability was calculated using the [3-(4,5-dimethylthiazol-2-yl)-2,5-diphenyltetrazolium bromide] (MTT) assay.

**2.7.2. Percentage of hemolysis (RBC breakdown).** Healthy people's red blood cells (RBCs) were isolated, and the process was carried out with minor alterations.[19] Briefly, 18 mL of 1× PBS solution was added to 2 mL of RBC suspension, and the mixture was centrifuged at 1500 rpm for 15 minutes. Following centrifugation, 100 μL of nanomaterial formulations, namely chitosan:PVA, EuME, EuME–AgNPs, PDGF/EuME–AgNPs and SBD–AgNPs, were added to 900 μL of RBC suspension, which was then centrifuged at 8000 rpm for 4 minutes. This mixture was kept under 5% $CO_2$ for 1 hour. For each sample (chitosan:PVA, EuME, EuME–AgNPs, PDGF/EuME–AgNPs and SBD-–AgNPs), the maximum dose concentration was maintained constant. Milli-Q water and PBS, which serve as positive and negative controls, respectively, were added to the freshly isolated RBCs. The absorbance levels were measured at 540 nm. The percentage of hemolysis was calculated[20,21] using eqn (4):

$$\text{Percentage of hemolysis (\%)} = ((\text{sample absorbance} - \text{negative control absorbance})/(\text{positive absorbance} - \text{negative control absorbance})) \times 100 \quad (4)$$

### 2.8. *In vitro* cytotoxicity assay

For cytotoxicity studies, the nanofiber samples (2 cm × 1 cm) were prepared in triplicate for each group, namely, control (chitosan:PVA) and experimental groups (EuME, EuME–AgNPs, PDGF/EuME–AgNPs and SBD–AgNPs) impregnated into nanofibrous mats based on the lower MIC value obtained. Primarily, in order to provide stability under water-based conditions, the nanofibrous mats were incubated for two hours at 80 °C in a pressurized and sealed oven. For the purposes of acetic acid neutralization and sample disinfection, the samples were cut into rectangular shapes measuring 2 cm × 1 cm and submerged in 70% ethanol for thirty minutes. The samples were washed with phosphate buffered saline (PBS) three times. Using the MTT assay, the potential cytotoxicity of the fabricated nanofibrous mats was studied. The 3T3 mouse fibroblast cell lines were used to determine the tissue biocompatibility of the nanofibrous mats. A sample of about 4 $cm^2$ was placed in 3 mL of serum-free medium and cultured at 37 °C for 1, 3 and 6 days. The control group consists of serum free culture medium without nanofibrous mats and incubated at 37 °C. Fibroblast cells were cultured in 50% DMEM supplemented with 10% FBS and 1% penicillin–streptomycin placed in an incubator at approximately 37 °C and 5% $CO_2$. Fibroblast cells were cultivated at a density of $1 \times 10^4$ cells per well in a 96-well plate. Then, 100 μL of 50% RPMI medium was added and the sample was incubated for 24 hours.[22]

To the incubated wells, 100 μL MTT was added and allowed to react for 2 hours. After 2 hours, the MTT reagent was then pipetted out, and the resultant violet formazan product was solubilized in 0.2 mL dimethyl sulfoxide for approximately 15 minutes at room temperature. The OD at 570 nm was read using a microplate reader. The percentage of cell viability of the control medium was defined as 100% and the percentage of cell viability of the samples was calculated with respect to the control value.

### 2.9. Release kinetics studies

Although various bioactive substances have been infused into nanofibrous mats,[23] due to their solubility, the controlled and sustained release of biopolymers still poses significant challenges. A strong binding capacity is conferred by the biopolymers linked to emulsions and particles, which ultimately leads to superior nanofiber encapsulation. The beaker method, which was conducted at 37 °C with a specific concentration of AgNP encapsulated nanofibers (EuME–AgNPs/CSNs and PDGF/EuME–AgNPs/CSNs) (0.35 g $L^{-1}$ Ag), was used to perform dialysis in order to evaluate the behavior of silver ion release

kinetics on simulated wound fluids (SWF). The dialysis bag ideally used for release kinetics studies possesses the following specifications based on the specified product: dialysis membrane-70 with a molecular weight cut-off of approximately 14 000 Da and a pore size of 2.5 nm. Approximately 1 cm × 1 cm pieces of the fabricated CSNs were placed inside the dialysis bag membrane and treated with SWF solutions at 7.4 (pH). Proteins such as bovine serum albumin (BSA) make up the majority of the chemical composition of SWF.[24] The dialysis procedure involved steady magnetic stirring at constant room temperature for specific intervals.[25] At predetermined intervals, the cumulative percentage of silver ion release was calculated at 400 nm.

### 2.10. *In vivo* diabetic wound healing

**2.10.1. Experimental design and the wound model.** The diabetic excision wound healing was carried out in STZ-induced Wistar albino rats (250–350 g). The male Wistar rats were procured with formal approval from the Institutional Animal Ethical Committee (IAEC) (VIT/IAEC/20/DEC2021/01). Three Wistar rats were housed in each polypropylene cage and provided with normal laboratory food (Lipton Feed, India) and water. Eight groups of three rats each ($n = 3$) were categorized for the excisional diabetic wound healing procedure: group I – control (no treatment); group II – vehicle control (citrate buffer); group III – chitosan:PVA/CSNs; group IV – EuME/CSNs; group V – EuME–AgNPs/CSNs; group VI – PDGF/CSNs; group VII – PDGF/EuME–AgNPs/CSNs; and group VIII – SBD–AgNPs/CSNs. According to several reports,[26,27] different compositions of STZ injections were administered along with normal chow or a high-fat diet. Type I diabetes was induced using a single high-dose intraperitoneal STZ injection (60 mg $kg^{-1}$) dissolved in 0.1 M citrate buffer, adjusted to pH 4. Prior to the STZ injection, the rats were allowed to fast overnight but were given access to water in order to prevent dehydration. STZ was injected the following morning with a standard amount of recovery diet.[28,29] At 72 hours after the STZ injection, a small incision was made on the rat tail using a sterile surgical blade. The required amount of blood was collected and absorbed onto blood glucose test strips using a glucometer to monitor the level of blood glucose. Upon diagnosis, if the level of blood glucose is greater than 250 mg $dL^{-1}$, the STZ-injected Wistar rat model is considered diabetic.

The diabetic rats were systematically anesthetized using chloroform prior to the excisional wound procedure.[30,31] At a distance of 4 cm from the ear area and 1.75 cm from the vertebral column, a distinct and clear excision wound area of 2 cm × 2 cm was made on the dorsal region of the body part. With the aid of transparent polyethene graph paper, the wound area was traced and measured as the initial day wound area. The treatment includes topical application of CSNs (*i.e.*, chitosan:PVA/CSNs, EuME/CSNs, EuME–AgNPs/CSNs, PDGF/CSNs, PDGF/EuME–AgNPs/CSNs and SBD–AgNPs/CSNs) on the excisional wound area. The percentage of wound contraction was monitored using graph paper on pre-determined days, *i.e.*, 0th, 3rd, 6th, 9th, 13th, 17th, 21st, 25th, and 30th days. Simultaneously, the level of blood glucose in STZ-induced Wistar rats was estimated post-wounding (0th, 20th, and 30th days) in order to determine the insulin level during the process. The percentage of wound contraction was calculated using the following equation:

$$\%\ \text{of wound contraction} = ((\text{initial day wound area} - \text{specific day wound area})/(\text{initial day wound area})) \times 100 \quad (5)$$

The zeroth day wound area was assigned as 100%, and the percentage of wound contraction (%) was calculated.

**2.10.2. Histopathological analysis.** The tissue samples collected from seven individual groups were fixed onto blank slides on specified days (7th, 14th, and 25th) for further staining. The skin samples with a diameter of 8 mm were removed using a punch biopsy and placed on Whatman No. 1 filter paper soaked in 10% (V/V) formalin solution for the purpose of tissue fixation. After a period of 24 hours, the tissues were dehydrated and embedded with paraffin. 5 μm thick sections of tissues were cut using a microtome. Hematoxylin and eosin staining was performed based on the staining protocol.

Masson's trichrome is a histochemical stain that detects the maturation of connective tissues in the respective groups. Blue corresponds to collagen, dark brown (or black) corresponds to cell nuclei, red corresponds to muscle fibers and keratin, and light pink corresponds to the cytoplasm. The organization and depth of the blue color differentiate the maturation of collagen fibers. Masson's trichrome staining was performed based on the staining protocol.

Immunohistochemical (IHC) slides for transforming growth factor beta (TGF-β) and neovascularization were prepared. For the expression of neovascularization, the tissue sections were incubated with anti-CD31 polyclonal antibody at a 1 : 100 PBS dilution, followed by incubation at 37 °C for 1 hour. The staining was performed based on the manufacturer's guidelines. For TGF-β staining, the tissue samples were incubated with the respective TGF-β1 antibody at a 1 : 100 PBS dilution following the same staining procedures. In order to effectively quantify the blood vessels and the number of stained cells for each individual sample, 10 high-power field (HPF) 400× magnifications on the sample sections were randomly viewed, and the cells were counted quantitatively. The TGF-β expression, inflammatory levels, and angiogenesis were evaluated. ImageJ software was used to obtain the proportion of blue color area in HPF representing the formation of collagen deposition.

### 2.11. Statistical analysis

Triplicate data were analyzed using Microsoft Excel and expressed as mean ± standard error. The statistical data were analyzed using analysis of variance (ANOVA). GraphPad Prism (GPD) V4.03 (San Diego, CA, USA) was used for the analysis.

## 3. Results and discussion

### 3.1. Synthesis and formation of PDGF-impregnated EuME–AgNPs systems

Microemulsions are pseudo-homogeneous, transparent, and thermodynamically stable dynamic structures comprising

lipophilic (essential oil) and hydrophilic (aqueous) phases.[32] These formulations possess the capacity to carry active biological molecules or agents to the targeted delivery site and exhibit longer shelf life, high surface area, definite droplet size, optical transparency and greater drug mobility characteristics.[33] The current work focuses on the formation of eugenol-based silver nanomaterials using Tween 80 as the surfactant, which possess non-toxic nature and biocompatible characteristics suitable for biomedical applications. Stable eugenol-based microemulsions were prepared using a range of surfactant ratios. Clear and transparent microemulsions were obtained. The transparent appearance of microemulsion formation at 1 : 5 determines a defined droplet size (nm) and a stable zeta potential (mV). EuME exhibited a hydrodynamic droplet size of 28.4 nm at pH 7 with a polydispersity index of 0.457. Zeta potential was determined to be −1.4 mV, and even after six months, the microemulsions proved to be kinetically stable. Using centrifugation, freeze–thaw, and heating–cooling cycles, the formulated EuME was put through a series of tests to determine its stability. The experimental results prove that the absence of phase separation and creaming confirms the stable formation of EuME formulations under different temperature variations. The formulated microemulsions were stored for a long time (roughly six months) in order to determine the kinetic stability of EuME. ''An increase in the concentration of surfactant gradually decreases the hydrodynamic droplet size of microemulsions''. The size and intensity of droplets are influenced by surfactants' chemical and steric structures. The probability of droplet coalescence is decreased by the formation of microemulsion at an appropriate low surfactant concentration, which is found to be acceptable for drug delivery applications.[34] The observed results proved to be consistent with the other research outcomes.[35,36] Hence, it has been observed that eugenol essential oil and Tween 80 work synergistically and are found to be more suitable for optimizing stable microemulsions.

Different volumetric concentrations of EuME (reducing or stabilizing agent) (1%, 3%, 5%, 7%, and 9%) were formulated with $AgNO_3$ in order to avoid aggregation of AgNPs. The statistical analysis using Box-Behnken design (BBD) demonstrated that polynomial models were found to be highly significant, indicating model reliability. $R^2$ values exceeding 0.95 indicate that over 95% shows variability in the SPR peak, particle size and yield efficiency (%). Significant effects were monitored not only for individual factors such as EuME concentration, temperature and reaction time, but also for interactions emphasizing relationships over nanoparticle synthesis. Table S1 shows the optimization process of nanoparticle synthesis using Box-Behnken design. Stable yellowish AgNPs were formed using 9% EuME after the suspension was incubated at 400 rpm for 40 hours as shown in Fig. S1(a). The reduction of silver ions ($Ag^+$) from $AgNO_3$ precursor to silver atoms ($Ag^0$) undergoing nucleation through eugenol, which serves as a bio-based reducing and stabilizing agent due to phenolic –OH groups, involves a chemical reaction, changing their surface charge from +1 to 0, leading to the formation of AgNPs. The homogenous micelle formation enhances particle stabilization, thereby preventing chemical aggregation by rendering surface capping properties and steric hindrance to AgNPs. The surface plasmon resonance (SPR) peak of EuME–AgNPs was observed at 412 nm as shown in Fig. S1(b). AgNPs' conversion efficiency demonstrates that the practical and theoretical yields of AgNPs (>99% and >96%) are equal. The presence of eugenol interacts with the surface of AgNPs through the phenolic hydroxyl group forming strong dipolar bonds with silver atoms. Under some conditions at higher pH, the partial ionization at the hydroxyl side imparts negative surface interactions, resulting in electrostatic repulsion between the particles. Thus, the combined effect of physical and chemical binding between eugenol and AgNPs prevents aggregation or further growth of particles, resulting in enhanced stability and longer shelf-life of AgNPs.[37] EuME–AgNPs possess a particle size of 38.5 nm, a zeta potential of −1.4 mV, and a polydispersity index of 0.342. The droplet size and polydispersity index of EuME–AgNPs were measured using the dynamic light scattering technique and the size distribution is graphically shown in Fig. S1(c). EuME and EuME–AgNPs possess equivalent zeta potential stability due to similar surface chemistry properties resulting in analogous electrostatic interactions in dispersion. Eugenol containing various functional groups such as methoxy ($-OCH_3$) and hydroxyl (–OH) interacts with the aqueous phase through partial ionization and hydrogen bonding, leading to the formation of surface charge. In the case of EuME, the surfactant containing the polar head groups interact at the oil–water interface, forming an electrical double layer stabilizing the droplets through electrostatic repulsion. During EuME–AgNP synthesis, silver ions get reduced and bind to the surface through various chemical mechanisms, such as hydrogen bonding, hydrophobic interactions and Ag–O coordination, where the lone pair electrons on the oxygen atom donate electron density to the vacant orbitals of silver atoms on the nanoparticle surface. Due to this, the synthesized AgNPs acquire a charge distribution and surface composition similar to EuME droplets. This similarity in surface interfacial chemistry leads to stable zeta potentials, reflecting the strength of electrostatic repulsion between the particles. As a result, both EuME and EuME–AgNPs exhibit equivalent colloidal stability. Usually, the zeta potential values of the synthesized AgNPs would be relatively as high as +30 mV due to their electrostatic stability as reported in some studies. In the current case, the zeta potential value was measured to be −1.4 mV, which may be due to steric hindrance provided by the co-surfactants and surfactants used in the microemulsion formulation, thereby preventing particle aggregation independent of strong electrostatic repulsion. Numerous studies reported that microemulsion/nanoemulsion based systems possess low zeta potential values (typically less than +10 mV), resulting in stable colloids due to steric hindrance.[38] Nanoparticles are distributed uniformly throughout the chemical formulation system when the polydispersity index value is less than 0.5. As observed using TEM, EuME–AgNPs possess a particle size of 25.2 ± 0.1 nm, which is smaller than the hydrodynamic particle diameter.

Using AAS analysis, it was found that the total mass concentration was 25.36 mg $L^{-1}$ and the optimal pH for EuME–AgNPs was 7.4. After storing the synthesized nanoparticles for a long time, the stability of EuME–AgNPs was examined. The synthesized nanoparticles were found to be stable even after a storage period of 6 months. No visible creaming, phase separation, turbidity or sedimentation was observed during the storage period. Furthermore, the distribution of droplet size, polydispersity index and zeta potential remained unchanged, confirming that, despite the low zeta potential value, the prepared formulations possess effective kinetic stability with respect to time duration. Some reports show that EuME–AgNPs using 1 mM $AgNO_3$ have a particle size between 10 and 20 nm, which demonstrates the toxicity and heterogeneity of nanoparticles in drug delivery due to their smaller particle size.[39] Hence, in the current study, the particle size of EuME–AgNPs was optimized between 35 and 40 nm, demonstrating the non-toxicity and homogeneity of nanoparticles. In order to support these findings, the percentage of cell viability of EuME–AgNPs using 3T3 fibroblast cell lines was determined to be approximately 98% with respect to the 6th day when compared to SBD–AgNPs, for which the value was only around 68% with respect to the 6th day as shown in Fig. 4(c). Although the particle size of SBD–AgNPs was comparatively less than that of EuME–AgNPs, the cytotoxicity experiments using 3T3 fibroblast cell lines proved their toxicity towards SBD–AgNPs. The results confirm that the cytotoxicity of AgNPs is solely size dependent, which has been well optimized for effective drug delivery applications. The susceptible microbial strains used for antimicrobial activity in earlier reports were *E. coli*, *S. aureus, P. aeruginosa* and *C. albicans*.[40] The mean particle size, thermodynamic stability, and yield efficiency of EuME–AgNPs were found to be efficient when compared with other studies.[41] Furthermore, in order to blend PDGF with the synthesized EuME–AgNPs in an equivalent proportion, varying concentrations (1%, 3%, 7%, and 9%) of platelet derived growth factor (PDGF) were impregnated with EuME–AgNPs at 500 rpm for 20 minutes in a magnetic stirrer to form a homogenous blended PDGF-impregnated EuME–AgNPs combination. Post impregnation, the encapsulation efficiency (%) of PDGF impregnated EuME–AgNPs was calculated to be 95%. The results suggest that there is effective encapsulation and loading of PDGF within EuME–AgNPs, indicating minimal loss of PDGF degradation during the encapsulation process. In addition, the percentage of encapsulation accelerates the oral bioavailability of PDGF and exhibits therapeutic action towards targeted drug delivery paradigms. Furthermore, the blended PDGF-impregnated EuME–AgNPs combination was fabricated along with the biopolymeric matrix (chitosan:PVA) using the coaxial electrospinning technique to form high-efficacy CSN by optimizing the concentration, flow rate, applied electric field, and tip–rotor interspace.

### 3.2. Effect of electrospinning parameters on core–sheath nanofibrous mats (CSNs)

Electrospun nanofibers possess long polymeric filaments that exhibit high surface area, controllable morphology, high porosity, high encapsulation efficiency, and high thermal and chemical stability.[42,43] Different concentrations of PVA (2%, 4%, 6%, 8%, and 10%, w/v), chitosan (1%, 3%, 5%, and 7%, w/v) : PVA (2%, 4%, 6%, 8%, and 10%, w/v) (chitosan:PVA/CSNs), EuME/CSNs (1%, 3%, 7%, and 9%, v/v), EuME–AgNPs/CSNs (1%, 3%, 7%, and 9%, v/v) and PDGF/EuME–AgNPs/CSNs (1%, 3%, 7%, and 9%, v/v) were obtained. The rationale for the selection of different concentrations of PVA, chitosan:PVA, EuME/CSNs, EuME–AgNPs/CSNs and PDGF/EuME–AgNPs/CSNs depends on the following criteria: studies prove that 9–10% w/v of PVA is found to be optimal for fabricating bead-free homogeneous nanofibrous mats with desired physicochemical properties.[44] In order to facilitate sustained release of polymers in diabetic wounds, a desired concentration of chitosan was proportionally optimized with PVA. 2–4% w/v of chitosan is considered, as these typical concentrations of chitosan balance the processability, viscosity, and thermal and mechanical properties, resulting in stable biobased nanofibrous mats.[45] Higher concentrations ranging between 5 and 9% v/v are potentially used for the nanofabrication process, which may be due to the antioxidant and antimicrobial properties of eugenol present in the nanofibrous mats. The concentration range fixed for EuME balances biological efficacy aligning with the studies ensuring therapeutic levels without disturbing the mechanical properties of nanofibrous mats.[46] The varying higher concentrations of EuME–AgNPs and PDGF/EuME–AgNPs ranging from 5 to 9% v/v were chosen for their sustained release of PDGF and EuME–AgNPs onto core–sheath nanofibrous mats by examining their threshold levels at higher concentrations without affecting the surface morphological structure of nanofibrous mats or causing any cytotoxicity.[47,48] The higher concentrations of growth factors enhance tissue regeneration and antimicrobial activity, thereby helping in stabilizing the bioactive agents present in the nanofibrous mats. Bead-free and homogeneous nanofibers were produced. Electrospinning parameters such as the flow rate, tip–rotor interspace, and applied electric field for different concentrations of PVA, chitosan:PVA/CSNs, EuME/CSNs, EuME–AgNPs/CSNs, and PDGF/EuME–AgNPs/CSNs, respectively, were proportionally optimized. According to the observed outcomes, the elemental weight percentage and fiber diameter gradually increase as the nanomaterial's concentration increases. These findings matched those of previous studies.[49] Among the different concentrations (2%, 4%, 6%, 8%, and 10%, w/v) of PVA, only 10% w/v showed homogeneous and bead-free nanofibrous mats (Fig. 1a).

PVA nanofibers are considered to be non-toxic, hydrophilic, and biocompatible semicrystalline biopolymers that possess excellent physicochemical properties such as water solubility, mechanical strength, and thermal characteristics.[50] Among the various proportionate ratios of chitosan:PVA/CSNs, only 3% w/v of chitosan and 10% w/v of PVA exhibited smooth nanofibrous mats with less clogging characteristics and bead-free nanostructures (Fig. 1e). PVA and chitosan impregnated electrospun nanofibers possess unique physicochemical characteristics such as high porosity, high surface area to volume ratio, pore

 

size within the nanorange and high flexibility for physical and chemical functionalization.[51] Among the different concentrations (1%, 3%, 7%, and 9%, v/v) of EuME, consistent and homogeneous nanofiber distribution was observed using 9% v/v of EuME, suggesting the impregnation of eugenol phenolic molecules with the surfactant incorporated on the biopolymeric matrix to produce EuME/CSNs. Morphological analysis was determined using SEM (Fig. 1i). Among the different concentrations (1%, 3%, 7%, and 9%, v/v) of EuME–AgNPs, uniform and blister-free nanofiber distribution was observed using 9% v/v of EuME–AgNPs, suggesting that the eugenol compound and silver complex were effectively encapsulated and integrated on the biopolymeric matrix to produce EuME–AgNPs/CSNs (Fig. 1m). Among various concentrations (1%, 3%, 7%, and 9%, v/v) of PDGF/EuME–AgNPs/CSNs, only 9% v/v exhibited smooth and homogenous nanofibrous mats, which suggested effective encapsulation and impregnation of PDGF as a surface capping agent in the fabrication of EuME–AgNPs as a core compound embedded on a biopolymeric matrix, and the morphological structure was determined using SEM (Fig. 1q).

Blended solutions of 10% w/v PVA, 3% w/v chitosan:10% w/v PVA, 9% v/v EuME, 9% v/v EuME–AgNPs, and 9% v/v PDGF/EuME–AgNPs were electrospun using the co-axial electrospinning technique. The translation speed, drum speed and temperature were kept constant at 65, 700 rpm and 37 °C, respectively. While maintaining the tip–rotor interspace (10 cm) and flow rate (0.25 mL $h^{-1}$) for pump 1 and the flow rate (0.2 mL $h^{-1}$) for pump 2, the applied electric field was increased from 15 kV to 25 kV. When an electric field of 15 kV was applied, a heterogeneous and constrictive distribution of nanofibers was observed; however, as the electric field was gradually increased to 25 kV, a homogenous and wider dispersion of nanofibers was observed. At an electric field of 25 kV, bead-free nanofibrous membranes were implanted on a biopolymeric complex to generate the electrospun nanofibers. The repulsive force created on the fluid jet during co-axial electrospinning unquestionably increases as the electrical field is increased, which results in a uniform distribution of nanofibers. The experimental observations show that the nanofibers are greatly influenced by electric fields, which have little impact on their structure and morphology. In several studies, similar observations have been reported.[52]

The tip–rotor interspace was varied between 5 and 25 cm. The applied electric field and flow rates for pumps 1 and 2 were maintained constant at 25 kV, 0.25 mL $h^{-1}$, and 0.2 mL $h^{-1}$, respectively. The translation speed, drum speed and temperature were kept constant at 65, 700 rpm and 37 °C, respectively. At an interspace of 5 cm, the nanofibrous mats were damaged, resulting in a heterogeneous distribution. The amount of beaded structure decreased as the interspace increased to 15 cm, resulting in a transparent nanofiber distribution. When the interspace was increased beyond 20 cm or up to 25 cm, slightly invisible and heterogeneous structures were observed. To construct efficacious nanofibrous structures, a tip–rotor interspace of 15 cm is sufficient for effective fabrication. The tip–rotor interspace and applied electric field were maintained constant by varying the flow rate in the range of 0.1 mL $h^{-1}$ to 0.7 mL $h^{-1}$ for both pumps 1 and 2. The flow rate in the electrospinning process greatly influences the structural morphology of nanofibrous mats.[52] In a typical co-axial electrospinning technique, the flow rate of the outer layer or fluid is always higher than the flow rate of the inner layer or fluid in order to play a wrapping role. In pump 1 (the core layer), the flow rate of the inner fluid was optimized at 0.13 mL $h^{-1}$, resulting in homogeneous and bead-free nanofibrous mats. Similarly, in pump 2 (the sheath layer), the flow rate of the outer fluid was optimized at 0.2 mL $h^{-1}$, which results in the formation of a smooth sheath layer. A uniform nanofiber distribution was observed at 0.13 and 0.2 mL $h^{-1}$ (for pumps 1 and 2, respectively), which leads to improved quality of the nanofibers. The experimental findings show that 0.13 mL $h^{-1}$ (flow rate – pump 1 – core layer) and 0.2 mL $h^{-1}$ (flow rate – pump 2 – sheath layer) were observed to be optimal values to fabricate efficacious nanofibrous mats. In tissue engineering systems, nanofibers made from diverse synthetic and biological polymers combined with wound-healing agents serve as ideal scaffolds. In order to achieve a wider and more uniform dispersion of the core–sheath nanofibrous matrix, the applied electric field, tip–rotor interspace, and flow rates for pumps 1 and 2 were optimized at 25 kV, 15 cm, 0.13 mL $h^{-1}$, and 0.2 mL $h^{-1}$, respectively. Apart from optimization of the flow rate, applied voltage and needle tip-to-collector distance, the needle diameter plays a crucial role in the uniformity and size distribution of nanofibrous mats. A desired needle diameter of 0.5 mm was used to produce uniform and bead-free core–sheath nanofibrous mats. The solvent of choice used for the electrospinning process affects the solution's viscosity and fiber morphology. A combination of acetic acid was used to prepare chitosan-based solutions which could influence the evaporation rate, volatility and fiber formation in order to ensure smooth and continuous nanofibrous mats. The type of collector employed for the electrospinning technique was a rotating drum collector, which influences fiber deposition and alignment. The rotating speed was adjusted to around 700 rpm in order to balance the nanofiber distribution and fiber alignment. A larger collector surface area creates a denser nanofibrous mat accommodating a higher deposition rate of fibers. For a final product to be fabricated, the collector surface area is dependent on the desired nanofiber density. Prior to the fabrication process, the blended solutions of PVA, chitosan:PVA, EuME, EuME–AgNPs and PDGF/EuME–AgNPs were magnetically stirred to facilitate uniform distribution of nanofibers, preventing aggregation affecting the distribution of nanofibers.

### 3.3. Characterization of core–sheath nanofibrous mats (CSNs)

**3.3.1. Determination of surface morphology and elemental analysis.** The structural surface morphology of CSNs was determined through field emission scanning electron microscopy (FESEM), and the elemental composition of CSNs was examined through energy dispersive X-ray analysis (EDAX). The synthesized CSNs were chemically crosslinked using 50% v/v glutaraldehyde vapor for 2 hours at room temperature. The crosslinked CSNs

were air-dried at 60 °C for a few hours. The surface morphology of CSNs before and after crosslinking was studied and is shown in Fig. 1a–t. The experimental results show that the 10% PVA matrix exhibited smooth and bead-free nanofibrous mats with an average fiber diameter of 120–150 nm. The fabricated nanofibers were found to be homogeneous in distribution, and bead-free nanostructures were observed in 10% PVA matrix complexes. The structural morphology of a 10% PVA matrix and the average nanofiber diameter (before crosslinking) are shown in Fig. 1a and b. The experimental results show that chitosan:PVA/CSNs revealed a monotonous distribution of nanofibers with slight bead structures and an average diameter of 130–190 nm. Although chitosan has been proportionately homogenized in the combination of chitosan:PVA core–sheath nanofibers, there will be a slight presence of beaded nanostructures, which does not affect the overall morphological distribution. The structural morphology of chitosan:PVA/CSNs and the average nanofiber diameter (before crosslinking) are shown in Fig. 1e and f. The results show that 9% of EuME/CSNs exhibited a homogeneous and smooth distribution of nanofibrous mats with an average diameter of 100–150 nm. The EuME droplets have been homogeneously functionalized on the biopolymeric matrix. The structural morphology of 9% EuME/CSNs and the average fiber diameter (before crosslinking) are shown in Fig. 1i and j. The results show that 9% of EuME–AgNPs/CSNs revealed the silver beaded structures of nanofibers embedded on the biopolymeric matrix and showed homogenous deposition of silver nanocomposites with an average fiber diameter of 100–180 nm. The synthesized AgNPs have been impregnated with EuME, and the structural morphology revealed that the silver complex has been functionalized on the nanofibrous mats and resulted in smooth nanofibrous structures. The structural morphology of 9% EuME–AgNPs/CSNs and the average fiber diameter (before crosslinking) are shown in Fig. 1m and n. The experimental results show that 9% of PDGF/EuME–AgNPs/CSNs exhibited a smooth and homogeneous distribution of nanofibrous mats with an average fiber diameter of 100–200 nm. Although there is impregnation of the growth factor with silver nanocomposites embedded in the biopolymeric matrix, there is uniformity in the distribution of nanofiber diameter. This shows that the PDGF-impregnated electrospun CSNs are structurally and morphologically stable, which makes them suitable for further characterization studies. The structural morphology of 9% PDGF/EuME–AgNPs/CSNs and the average fiber diameter (before crosslinking) are shown in Fig. 1q and r.

The structural morphology of electrospun nanofibers has been determined using FESEM and EDAX after the crosslinking procedure. The morphological results indicate that the 10% PVA matrix exhibited smooth and bead-free nanostructures even after crosslinking with glutaraldehyde solution, with an average fiber diameter of 130–200 nm. PVA-impregnated core–sheath electrospun nanofibers exhibited excellent mechanical strength, porosity, flexibility, rigidity, feasibility, biocompatibility and biodegradability for further biomedical applications. The structural morphology of the 10% PVA matrix and the average fiber diameter (after crosslinking) are shown in Fig. 1c and d. Chitosan:PVA/CSNs exhibited an equal and smooth distribution of nanofibers even after the crosslinking process, along with greater mechanical strength and porosity with an average diameter of 150–200 nm. Although there is impregnation of chitosan, the fabricated nanostructures were found to be uniform, and there is no breakage in the fabrication of core–sheath nanofibers. The structural morphology of chitosan:PVA/CSNs and the average fiber diameter (after crosslinking) are shown in Fig. 1g and h. The morphological images of 9% EuME/CSNs revealed that the impregnation of the eugenol compound into the biopolymeric matrix was stable, and the fabricated core–sheath nanofibers were also uniform and smooth, which resulted in stable physicochemical properties and an average diameter of 180–200 nm even after crosslinking. Crosslinking with glutaraldehyde does not disturb the fabrication of smooth CSNs, which confirms their mechanical stability. The structural morphology of 9% EuME/CSNs and the average fiber diameter (after crosslinking) are shown in Fig. 1k and l. The experimental results indicate that 9% of EuME–AgNPs/CSNs exhibited a monotonous distribution of electrospun bead-free CSNs, which exhibited greater mechanical strength and biocompatibility with an average diameter of 180–220 nm. Although there is impregnation of silver nanoparticles along with EuME, the diameter of CSNs does not change, which results in uniform nanofiber distribution. The presence of the silver complex prevented the breakage of nanofibrous mats, which resulted in a uniform distribution of nanofibrous mats. The structural morphology of 9% EuME–AgNPs/CSNs and the average fiber diameter (after crosslinking) are shown in Fig. 1o and p. The experimental results indicate that 9% PDGF/EuME–AgNPs/CSNs exhibited a uniform distribution of electrospun nanofibrous mats with bead-free nanostructures embedded on the chitosan:PVA biopolymeric matrix with an average nanofiber diameter of 160–210 nm even after crosslinking with glutaraldehyde solution. Impregnation of the growth factor into the biopolymeric matrix could inevitably enhance the morphological structures and porosity of CSNs without any shrinkage in the fabricated nanofibers. The structural morphology of 9% PDGF/EuME–AgNPs/CSNs and the average fiber diameter (after crosslinking) are shown in Fig. 1s and t.

The elemental composition of the CSNs (9% EuME–AgNPs/CSNs and 9% PDGF/EuME–AgNPs/CSNs) was determined using energy dispersive X-ray analysis (EDAX). Fig. 1u and v show the elemental composition of 9% EuME–AgNPs/CSNs. The weight percentage (wt%) was found to be 0.5 for silver (Ag), 65.9 for carbon, and 33.6 for oxygen before the crosslinking process (Fig. 1u). Even after crosslinking, the weight percentage (wt%) of silver was maintained, which was approximately 1.9, and that of oxygen was found to be 98.1 (Fig. 1v). The elemental composition of 9% PDGF/EuME–AgNPs/CSNs was determined (Fig. 1w and x). The weight percentage (wt%) of silver (Ag) was found to be 2.0 and that of oxygen was found to be 98.0 before the crosslinking process (Fig. 1w). Even after crosslinking, the weight percentage (wt%) of silver was maintained, which was approximately 2.8, and that of oxygen was found to be 97.2 (Fig. 1x).

**3.3.2. Determination of internal morphology and crystallinity.** The internal core–sheath structure of nanofibrous mats

was evaluated using transmission electron microscopy (TEM), and the crystallinity of the nanofibrous mats was determined using selected area electron diffraction (SAED) patterns. Fig. 2 presents the internal morphology and crystallinity of core–sheath nanofibers. In figure, the flow of the electron beam passing through different areas of the nanofiber structure shows dark and light phases, in which the darker areas represent the core layer and the lighter areas represent the sheath layer.

Fig. 2a–d present the internal morphology of EuME/CSNs at different magnifications. Fig. 2a shows the impregnation of EuME into the internal structure of core–sheath nanofibers, which is represented by yellow arrows. The fabricated CSNs were clearly functionalized with EuME, resulting in bead-free and homogeneous nanofibrous mats. Fig. 2b presents the distinct core–sheath structure of EuME/CSNs. The lighter area of the nanofibers shows the sheath layer, and the darker area of the nanofibers represents the core layer. The deposition of EuME on the internal structure of CSNs is clearly depicted (Fig. 2b). Fig. 2c and d show the overall internal microscopic view of EuME/CSNs, indicating the impregnation of eugenol-based functional compounds and a distinct core–sheath nanofibrous structure. Fig. 2e presents the crystallinity of EuME/CSNs determined using SAED patterns. SAED can be used to measure the lattice constants and crystal orientation of the sample. The fabricated EuME/CSNs were found to be amorphous in structure due to the broader distribution of the selected area diffraction (Fig. 2e). The EuME-impregnated nanofibers possess an indefinite shape and structure, which may be due to the heterogeneous distribution of the eugenol-emulsified compounds on the nanofibrous matrix.

Fig. 2f–i present the internal morphology of EuME–AgNPs/CSNs at different magnifications. Fig. 2f and g show the homogenous dispersion of EuME–AgNPs on the biopolymeric matrix. The metallic AgNP complex on the nanofibrous matrix was found to be uniform and exhibited bead-free distribution, which could enhance the encapsulation efficiency of the nanofibrous scaffold. Fig. 2h and i show the distinct core–sheath structure, in which the lighter areas denote the sheath layer impregnated with chitosan and the darker areas denote the core layer, which is composed of EuME–AgNPs and PVA, represented by yellow arrows. Fig. 2j presents the crystallinity of EuME–AgNPs/CSNs determined using SAED patterns. The fabricated EuME–AgNPs/CSNs were found to be crystalline in structure due to the narrow distribution of the selected area diffraction (Fig. 2j). The nanofibers impregnated with EuME–AgNPs possess a definite shape and structure coupled with a biopolymeric matrix, which may be due to the uniform distribution of AgNPs in the nanofibrous mats. Fig. 2k–n present the internal morphology of PDGF/EuME–AgNPs/CSNs at different magnifications. Fig. 2k shows the clear and distinct encapsulated PDGF/EuME–AgNPs as the core layer, surrounded by the sheath layer, which is composed of chitosan, represented by yellow arrows. The experimental findings proved to be consistent with other research studies.[53] Fig. 2l and m show the overall internal microscopic view of PDGF/EuME–AgNPs. Fig. 2n presents

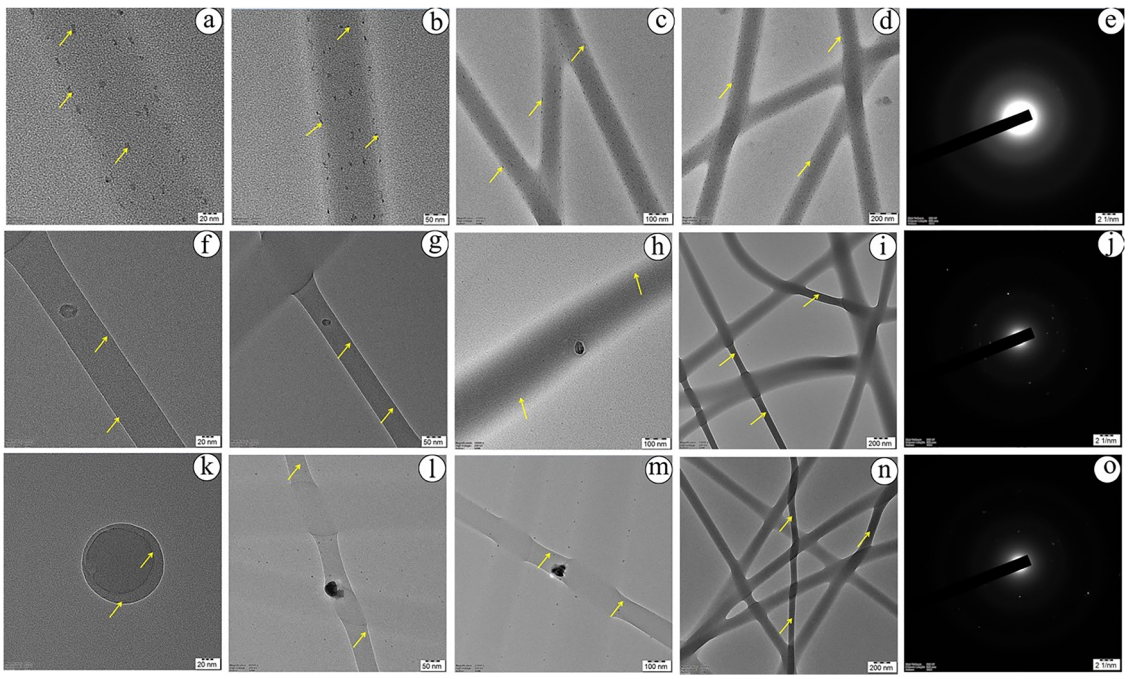


Fig. 2 Internal morphology (HRTEM) and crystallinity (SAED pattern) of core–sheath nanofibrous mats (CSNs). (a–d) Internal nanofibrous structure of EuME/CSNs using HRTEM at different magnifications, (e) determination of the crystallinity of EuME/CSNs using the SAED pattern, (f–i) internal nanofibrous structure of EuME–AgNPs/CSNs using HRTEM at different magnifications, (j) determination of the crystallinity of EuME–AgNPs/CSNs using the SAED pattern, (k–n) internal nanofibrous structure of PDGF/EuME–AgNPs/CSNs using HRTEM at different magnifications, and (o) determination of the crystallinity of PDGF/EuME–AgNPs/CSNs using the SAED pattern.

the homogeneous distribution of the PDGF-impregnated core–sheath nanofibrous structure with clear internal structural morphology, which helps to enhance the efficiency of the impregnated growth factor, resulting in sustained or controlled release of PDGF/EuME–AgNPs/CSNs in the biological system. Fig. 2o presents the crystalline nature of PDGF/EuME–AgNPs/CSNs determined using SAED patterns. The fabricated PDGF/EuME–AgNPs/CSNs were found to be crystalline in structure due to the narrow and clear distribution of the selected area diffraction (Fig. 2o). The PDGF-impregnated EuME–AgNPs possess a definite crystal size, shape, and structure coupled with a biopolymeric matrix, which may be due to the smooth and bead-free structure of the core complex that could enhance the sustained or controlled release of the encapsulated growth factor and the efficiency of the nanofibrous scaffold in the biological system.

**3.3.3. Identification of functional groups using FTIR analysis.** FTIR is an analytical technique used to identify the conformational functional groups coupled with the molecular bonds present in the respective chemical compounds of the fabricated nanomaterial.[54] The FTIR spectrum of the fabricated CSNs is shown in Fig. S2(i).

Fig. S2(i)a displays the FTIR spectrum of the fabricated PVA matrix, which shows predominant peaks at 3314.07 $cm^{-1}$ due to O–H stretching and 1725.97 $cm^{-1}$ due to –C═O bonding that represent the definite characteristic peaks of the entire PVA polymeric blend. The prominent peaks of the PVA matrix were observed at 1439.60 $cm^{-1}$ and 1377.88 $cm^{-1}$, which were due to the bending of O–H bonds, and 2943.80 $cm^{-1}$ due to C–H stretching; minor peaks observed at 950.73 $cm^{-1}$, 848.52 $cm^{-1}$ and 615. 18 $cm^{-1}$ were due to C–H bending. The characteristic peaks observed at 1258.32 $cm^{-1}$ and 1097 $cm^{-1}$ were due to C–O stretching in PVA nanofibers. The characteristic peaks indicate the presence of carboxylic acid and hydroxyl groups in the fabricated PVA-loaded nanofibrous scaffolds, which were found to be similar to other research outcomes.[55,56] Fig. S2(i)b displays the characteristic peaks of chitosan:PVA/CSNs observed using the FTIR spectrum. The spectra of chitosan showed predominant characteristic peaks at 523.57 $cm^{-1}$ (out-of-plane C–O bending), (out-of-plane NH bending) and 3315.03 $cm^{-1}$ (OH stretching). The band observed at 1599.66 $cm^{-1}$ is assigned to NH bending ($NH_2$) (amide II), and a minor peak observed at 1663.60 $cm^{-1}$ is assigned to C═O stretching (amide I) O═C–NHR. The band observed at 2945.73 $cm^{-1}$, 1433.81 $cm^{-1}$ and 1252.53 $cm^{-1}$ was attributed to $CH_2$ bending due to the presence of the pyranose ring. The peak observed at 1376.92 $cm^{-1}$ was strongly assigned to the presence of $CH_3$ wagging. As shown in Fig. S2(i)b, the increase in PVA concentration in the blended chitosan:PVA/CSNs caused a decrease in the band intensity from (amide II) NH bending at 1599.66 $cm^{-1}$ of chitosan. Additionally, an increase in the CH group was observed at 2945.73 $cm^{-1}$ as the content of PVA increases. A remarkable shift for the characteristic peak at 1095.36 $cm^{-1}$ to the highest wave number confirmed the efficient fabrication of combined chitosan:PVA/CSNs. The outcomes turned out to be consistent with earlier research findings.[57,58] For the FTIR spectrum of EuME/CSNs shown in Fig. S2(i)c, eugenol shows signature peaks between 850.45 $cm^{-1}$ and 1258.32 $cm^{-1}$ that correspond to the C═C region. Additionally, sharp characteristic peaks at 1652.69 $cm^{-1}$ and 1551.45 $cm^{-1}$ were observed due to C═C stretching of the aromatic moiety. The obtained FTIR spectrum was found to be in similar agreement with the reported eugenol spectrum. In the case of EuME, the impregnation of Tween 80 exhibited significant peaks at around 3680.47 $cm^{-1}$ (OH-stretching), 2931.26 $cm^{-1}$ ($CH_2$-stretching), 1735.62 $cm^{-1}$ (C═O-stretching), and 1652.69 $cm^{-1}$ (HOH-bending). The obtained eugenol-based FTIR spectrum was found to be similar to the reported spectrum of eugenol.[59,60] This confirms the formation of EuME using Tween 80 as an emulsifying agent to form stable microemulsions. The synthesized microemulsions have been electrospun into efficacious CSNs, and functionalization was confirmed by FTIR. In the case of EuME–AgNPs/CSNs, the hydroxyl bond observed at 3310.21 $cm^{-1}$ and 3748.93 $cm^{-1}$ is due to O–H stretching; a strong band observed at 2365.26 $cm^{-1}$ contributes to C═N═O asymmetric stretching vibration; a band at 1378.85 $cm^{-1}$ revealed C–H deformation, confirming the presence of the eugenol–methyl organic compound; the vibration observed at 1653.66 $cm^{-1}$ contributes to the formation of aromatic bonds and C═C stretching; 1732.72 $cm^{-1}$ signifies the formation of carboxylic acid and C═O stretching; and 1264.11 $cm^{-1}$ corresponds to the formation of phenolic hydroxyl and C–O stretching, as depicted in Fig. S2(i)d. These findings matched those of earlier reports. In addition, a stretching vibration observed at 1436.70 $cm^{-1}$ is attributed to $CH_2$ bending due to the occurrence of the pyranose ring, and 1099.22 $cm^{-1}$ contributes to a remarkable shift and confirms the presence of chitosan and PVA in EuME–AgNPs/CSNs. The FTIR spectrum of PDGF/EuME–AgNPs/CSNs is shown in Fig. S2(i)e. PDGF-BB peaks were observed at 1540.84 $cm^{-1}$ due to primary amine groups (–$NH_2$–) and the spectrum displayed absorption bands at 832.13 $cm^{-1}$, 928.55 $cm^{-1}$ and 1025.94 $cm^{-1}$ that mainly represent characteristic peaks of greater intensity due to repeated pyranose rings interferes with the ethereal bond C–O–C.[61] The hydroxyl bond observed at 3747.97 $cm^{-1}$ is due to O–H stretching; a strong vibration observed at 2365.26 $cm^{-1}$ contributes to C═N═O asymmetric stretching; and 1732.72 $cm^{-1}$ signifies the formation of carboxylic acid and C═O stretching, which confirms EuME–AgNPs/CSNs in the fabricated PDGF-BB impregnated EuME–AgNPs/CSNs. The band observed at 1540.84 $cm^{-1}$ is assigned to NH bending ($NH_2$) (amide II), and characteristic peaks at 1025.94 $cm^{-1}$ are due to C–O stretching formation, which confirms chitosan:PVA/CSNs as a base biopolymeric matrix in the fabrication of PDGF/EuME–AgNPs/CSNs. Thus, effective fabrication of PDGF/EuME–AgNPs/CSNs confirms the presence of the functional groups of chitosan:PVA/CSNs and EuME–AgNPs in the nanofibrous scaffold matrix.

**3.3.4. Determination of crystalline patterns using XRD analysis.** XRD is regarded as an extensive analytical technique that provides structural information on the crystal structure, preferred orientation, chemical composition, and layer thickness.[62] The XRD spectrum of the fabricated CSNs is shown in Fig. S2(ii). Fig. S2(ii)(a) displays the XRD spectrum of the fabricated pure PVA matrix, which showed predominant peaks

at $2\theta \approx 20.1^\circ$, $38.2^\circ$ and $45.1^\circ$. The significant crystalline peaks of the fabricated pure PVA matrix were mainly due to the string intra- and intermolecular bonding.[56,63] The XRD spectrum in Fig. S2(ii)(b) displays the characteristic peaks of chitosan:PVA/CSNs. The XRD pattern confirmed that chitosan exhibited two predominant peaks at $2\theta \approx 18.3^\circ$ and $22^\circ$, which are due to the inclusion of chitosan in the fabricated chitosan:PVA/CSNs. A significant peak observed for PVA showed crystallinity peaks at $2\theta \approx 20.1^\circ$, $38.9^\circ$ and $45^\circ$, which were due to the intermolecular bonding. Collectively, the XRD pattern reveals the presence of a combination of chitosan and PVA in the chitosan:PVA/CSNs blended matrix.[64,65]

The crystalline patterns characteristic of nanocomposites and nanofibers can be analyzed using XRD patterns.[66] The peaks observed at $2\theta \approx 65^\circ$ and $78^\circ$ in conjunction with the mild diffraction peaks at $2\theta \approx 20^\circ$ and $38^\circ$–$45^\circ$ indicate the presence of channel-type EuME/CSNs crystals that were successfully impregnated on the chitosan:PVA/CSNs biopolymeric matrix. The presence of eugenol in the matrix was determined by a variation in the diffraction peak of EuME/CSNs at $2\theta \approx 18^\circ$–$28^\circ$. The EuME-fabricated CSNs were observed to lack crystalline characteristics, yet structural analysis supported the compounds' aromatic composition as shown in Fig. S2(ii)(c). The experimental findings were observed to be similar to those of the synthesis and characterization of magnetite-functionalized eugenol composites.[59] Fig. S2(ii)(d) clearly shows the XRD patterns of EuME–AgNPs/CSNs. The remarkable diffraction peaks observed at $2\theta \approx 20^\circ$, $39^\circ$ and $45^\circ$ reveal the presence and impregnation of chitosan and PVA in the fabricated EuME–AgNPs/CSNs nanofibrous mats. The diffraction peaks observed at $2\theta \approx 65^\circ$ and $78^\circ$ indicate the formation of channel-typed crystals in eugenol-based nanocomposites. These variant diffraction peaks were closely associated with five different crystal planes of metallic silver: (2 0 0), (3 1 1), (1 1 1), (2 2 0), and (2 2 2). The experimental results determined that the AgNPs formed were regarded as elements of the face-centered cubic structure.[67] In addition, the peak associated with $Ag_2O$ was primarily not observed, which indicates the reduction of $Ag^+$ to elemental silver in the preparation process; moreover, no other reactions occurred. The XRD patterns of PDGF-impregnated EuME–AgNPs show significant peaks of PDGF at $2\theta \approx 30^\circ$ to $40^\circ$, which confirms the impregnation of the growth factor into the fabricated EuME–AgNPs/CSNs nanofibrous mats as shown in Fig. S2(ii)(e). The findings were consistent with other research studies.[68] The presence of chitosan:PVA in the synthesized CSNs is determined by the broad diffraction peaks at $2\theta \approx 65^\circ$ and $78^\circ$ along with salient diffraction deviations at $2\theta \approx 20^\circ$, and the presence of EuME confirms the presence of aromatic structures in PDGF-impregnated EuME–AgNPs/CSNs. Additionally, the variant diffraction peaks indicate the presence and identification of elemental silver in the face-centered cubic structure of the fabricated mat. Other diffraction peaks were not observed, which confirms the complete reduction of $Ag^+$ to elemental silver.

### 3.3.5. Mechanical behaviour of core–sheath nanofibrous mats (CSNs)

*3.3.5.1. Tensile testing.* The mechanical testing of nanofibrous materials reflects the interrelationship between deformation and its dynamic responses to an applied force or load. Important mechanical properties include tensile strength, material strength, ductility, hardness, flexibility, contact angle, stiffness, water uptake, weight loss, and porosity.[69] The breaking strain (%) was determined to be 120, 110, 121, 105, and 123 for the PVA matrix, chitosan:PVA/CSNs, EuME/CSNs, EuME–AgNPs/CSNs, and PDGF/EuME–AgNPs/CSNs as shown in Fig. 3a. The PVA matrix, chitosan:PVA/CSNs, EuME/CSNs, EuME–AgNPs/CSNs, and PDGF/EuME–AgNPs/CSNs were found to have ultimate stress values of 0.4, 0.6, 0.75, 0.8, and 1.2 MPa as shown in Fig. 3a.

When compared to chitosan:PVA/CSNs, the PVA matrix showed greater strain (%) because of its superior mechanical strength and flexibility. Lou *et al.*[70] determined that PVA has a high potential to fabricate fiber-forming properties and is resistant to solvents. PVA nanofibrous webs possess high flexibility and tensile strength. The experimental results obtained for the PVA matrix proved to be consistent with other study findings.[70] Koosha *et al.*[71] found that the tensile strength decreased for chitosan-impregnated nanofibrous mats, and the composite material was broken at lower stress and extension. The breaking strain (%) of chitosan:PVA/CSNs was consistent with the other research findings.[71] Although the addition of chitosan reduces the extension and elongation of nanofibers, the impregnation of EuME increases the flexibility and stiffness of EuME/CSNs, which could eventually accelerate the mechanical strength of the nanocomposite. Ardekani *et al.*[72] reported that elongation at break (%) values accelerate in the presence of essential-oil based microemulsions when compared to nanofibrous mats in the absence of essential oils. It is observed that the presence of essential oil-based microemulsions and cross-linking of nanofibers does not affect the tensile properties of the composite material. The breaking strain (%) of EuME/CSNs was found to be consistent with other research findings.[72] Upon the addition of PDGF into EuME–AgNPs/CSNs, the ultimate strain (%) takes a longer time to break when compared to the PVA matrix, chitosan:PVA/CSNs, EuME/CSNs, and EuME–AgNPs/CSNs, which proves the mechanical stability and flexibility of PDGF/EuME–AgNPs/CSNs. Asiri *et al.*[73] determined that growth factors derived from the classification of natural elastin and fibers enhanced the elasticity and yield strength of nanofibrous mats, thereby increasing the elongation at break (%). It was found that the breaking strain (%) of PDGF/EuME–AgNPs/CSNs was consistent with other research findings.[73] Tensile testing provides information about the yield strength, force or stress required to break a composite material and the ductility of the nanofiber composite. Due to the natural polymer chitosan's ability to endure pressure, when it was impregnated with a synthetic polymeric matrix, it was found that the ultimate stress (MPa) of the resulting chitosan:PVA/CSNs was higher than that of the PVA matrix. Upon impregnation of growth factor (PDGF) into EuME–AgNPs/CSNs, the ultimate stress (MPa) of PDGF/EuME–AgNPs/CSNs was comparatively low when compared to the other fabricated nanofibers. This indicates the flexibility and mechanical stability of PDGF/EuME–AgNPs/CSNs when ultimate force or load is applied.

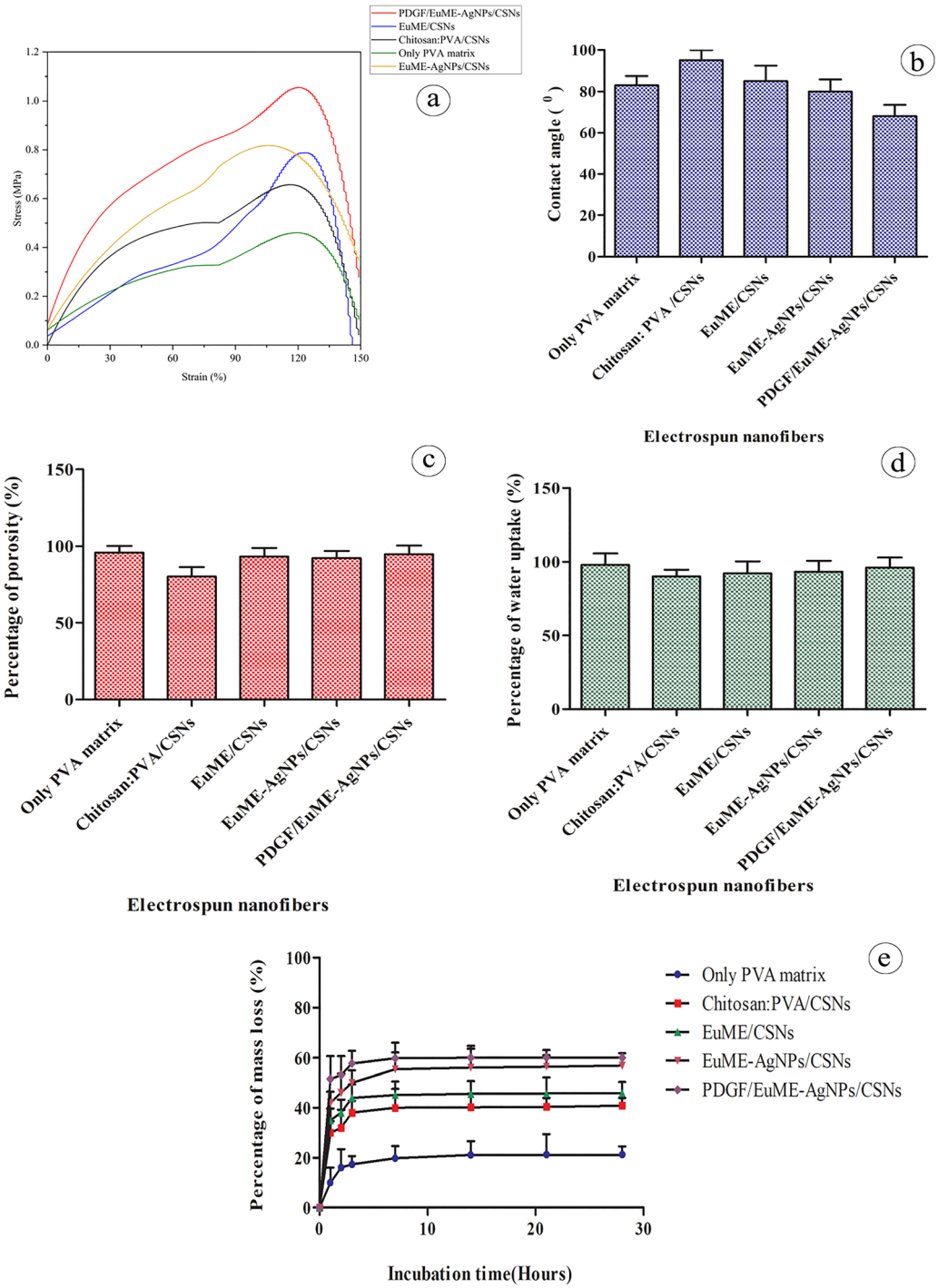


Fig. 3 Determination of the mechanical properties of core–sheath nanofibrous mats (CSNs): (a) strain *vs.* stress curves (tensile testing) of core–sheath nanofibrous mats (CSNs), (b) measurement of the contact angle (°) of core–sheath nanofibrous mats (CSNs), (c) determination of the porosity (%) of core–sheath nanofibrous mats (CSNs), (d) determination of the water uptake (%) of core–sheath nanofibrous mats (CSNs), and (e) determination of the mass loss percentage (%) of core–sheath nanofibrous mats (CSNs).

*3.3.5.2. Water contact angle.* Contact angle measurements play a vital role in nanofibrous membranes as they determine the hydrophilicity and fouling tendency of nanofibers. Studies have proven that membrane properties such as porosity, pure water permeation (PWP), and pore size of a nanofibrous membrane affect the contact angle. In a biological environment, the presence of hydrophilic amino acids in the cell membrane or the cell wall exhibits a strong affinity between cell wall proteins and hydrophilic surfaces.[74] Fig. 3b shows the water contact angle of the nanofibers. Hydrophilic functional groups are present in PVA-impregnated nanofibers, which have a contact angle of 83°. Chitosan:PVA/CSNs are physicochemically different from the other

materials because of the increase of water contact angle to 95° and the decrease in hydrophilicity that occur after chitosan impregnation of PVA nanofibers. The impregnation of natural polymers like chitosan with PVA-impregnated nanofibers reduces the hydrophilicity of composite materials due to the stiffness and ductility of the natural polymer. The findings were consistent with other research findings.[75] Fig. 3b shows the water contact angle measurement of EuME/CSNs and EuME–AgNPs/CSNs at 85° and 80°, respectively. The impregnation of EuME and EuME-based AgNPs along with chitosan:PVA/CSNs increases the wettability and hydrophilicity of nanofibrous mats, thereby decreasing the water contact angle. In the biological milieu, the wettability of nanocomposites is crucial for promoting cell adhesion and proliferation. Findings from previous studies were consistent with the reported results.[76] The incorporation of PDGF causes the nanofibrous mats to become more hydrophilic by reducing the water contact angle to 68° (Fig. 3b), which was accompanied by the presence of amine and hydroxyl groups in the GFs, eventually tailored by PDGF/EuME–AgNPs/CSNs focusing on greater wettability. These results were found to be similar to the contact angle measurements in the previous studies.[73]

*3.3.5.3. Porosity.* CSNs exhibit greater porosity by facilitating gaseous and nutrient exchange, which results in sustained drug delivery. The porosity of core–sheath nanofibrous materials, namely the PVA matrix, chitosan:PVA/CSNs, EuME/CSNs, EuME–AgNPs/CSNs, and PDGF/EuME–AgNPs/CSNs, was observed to be 95.8, 80.2, 93.2, 92.1, and 94.7, respectively. The porosity of the fabricated nanofibers lies in the range of 85–95%, which favors easy permeability and absorption capacity. As shown in Fig. 3c, the porosity of the PVA matrix increases due to its unique hydrophilic nature and wettability. The porosity of chitosan:PVA/CSNs decreases due to the addition of a natural polymer like chitosan, which exhibits defined physicochemical properties. Although the porosity of chitosan:PVA/CSNs decreases slightly when compared to the PVA matrix, the fabricated chitosan:PVA/CSNs are advantageous for cell proliferation and adherence. The porous nature may be due to the meso-structural combination of nanofibers.[77] From Fig. 3c, it can be concluded that EuME/CSNs, EuME–AgNPs/CSNs, and PDGF/EuME–AgNPs/CSNs are equally porous and efficient in gaseous and nutrient exchange. Similarly, the mesoporous structure of EuME–AgNPs/CSNs makes them an ideal vehicle for delivering growth factors.[78] Hence, the fabricated core–sheath nanofibers were found to have high porosity.

*3.3.5.4. Water uptake.* Appropriate water absorption plays a dynamic role in the wound healing process. The presence of moisture content in the wound bed stimulates cell migration and secretes cytokines, which in turn increase the cell attachment and adhesion, eventually resulting in the formation of native extracellular matrix (ECM). Fig. 3d shows the percentage of water uptake of the PVA matrix, chitosan:PVA/CSNs, EuME/CSNs, EuME–AgNPs/CSNs, and PDGF/EuME–AgNPs/CSNs. The percentages of water absorption and water uptake were observed to be 98%, 90%, 92.3%, 93.3%, and 96%, respectively. The percentage of water uptake in the PVA matrix was greater due to the amine and hydroxyl groups present in the synthetic polymeric matrix when compared to chitosan:PVA/CSNs, which may be due to the presence of hydrophobic groups. The impregnation of EuME/EuME–AgNPs into a biopolymeric matrix provides an excellent platform for cell proliferation and growth because the nutrients and bioactive components present in the essential oil can flow up easily and reach the cells when they are in need of nutrients and oxygen. On the other side, appropriate water uptake promotes slow degradation of the scaffold under wet conditions, which is a vital factor in tissue engineering.[79] Impregnation of PDGF with EuME–AgNPs/CSNs results in high water uptake ability, which may be due to the hydrophilic nature of PVA and the interconnected porous structure of core–sheath nanofibers. Nanofibrous membranes containing growth factors facilitate the absorption of wound exudate from the respective wound sites, resulting in easy permeability of nutrients and oxygen to the living cells. These findings were in line with other research publications.[80]

*3.3.5.5. Mass loss.* The percentage of mass loss of the PVA matrix, chitosan:PVA/CSNs, EuME/CSNs, EuME–AgNPs/CSNs, and PDGF/EuME–AgNPs/CSNs is shown in Fig. 3e. The percentage of mass loss was monitored at different time intervals, namely 0, 1, 2, 3, 7, 14, 21, and 28 hours. During 28-hour immersion in PBS solution, the PVA matrix, chitosan:PVA/CSNs, EuME/CSNs, EuME–AgNPs/CSNs, and PDGF/EuME–AgNPs/CSNs showed mass loss values of 21.22%, 40.94%, 45.92%, 56.8%, and 60.36%, respectively. The experimental results reveal that the impregnation of chitosan into the PVA matrix results in a mass loss due to the hydrophobicity of the natural polymer when compared to the pure PVA matrix. This may be due to the degradation of the oxygen-containing functional groups on the biopolymeric matrix. The experimental findings show that, with respect to time, the percentage of mass loss of PDGF/EuME–AgNPs increases in comparison to EuME and EuME–AgNPs. This may be due to the presence of the growth factor in the nanocomposite, which facilitates faster permeability, absorption capacity, and wettability, eventually resulting in an increase in the percentage of mass loss, which was similar to other findings.[81]

### 3.4. *In vitro* antibacterial activity

Eugenol is regarded as the major organic compound that has greater antibacterial activity and diabetic wound healing efficacy.[82] The zone of inhibition of nanomaterials was determined using well diffusion assays against *S. aureus* and *P. aeruginosa* as shown in Fig. S3(i), Fig. S3(ii) and Fig. S4 and tabulated in Table S2. When compared to the other groups, PDGF-impregnated eugenol-based nanomaterials exhibited greater antimicrobial efficacy. Hence, growth factors play an important role in enhancing the antibacterial efficacy of susceptible strains. In treatment against *S. aureus*, uncapped AgNPs exhibited a minimal zone of inhibition of 5 mm, which was due to the uncapping properties of the silver nanomaterial.

Chitosan:PVA showed a value of 3 mm, which was even less than that of uncapped AgNPs due to the absence of the core compound. Various concentrations of EuME (1%, 3%, 7%, and 9%) were treated against *S. aureus*, and the zone of inhibition (mm) was 2 mm, 4 mm, 6.5 mm and 7.5 mm as shown in Fig. S3(i)(b). Inclusion of the eugenol compound in the eugenol composite material enhanced EuME's efficiency, comparable to that of uncapped AgNPs. Varying concentrations of EuME–AgNPs (1%, 3%, 7%, and 9%) were treated against *S. aureus*, and the zone of inhibition (mm) was 7 mm, 9 mm, 13 mm, and 16 mm, respectively, as shown in Fig. S3(i)(c), which was comparatively greater than that of EuME due to the presence of eugenol-based AgNPs associated with the biopolymeric matrix. PDGF was tested against *S. aureus* at varying concentrations of 1%, 3%, 7%, and 9% and the zone of inhibition (mm) was 3 mm, 7 mm, 11 mm, and 13 mm, respectively, as shown in Fig. S3(i)(d). Varying concentrations of PDGF/EuME–AgNPs (1%, 3%, 7%, and 9%) were tested, and the zone of inhibition (mm) was 14 mm, 18 mm, 19 mm, and 21 mm, respectively, as shown in Fig. S3(i)(e), which shows that PDGF-impregnated EuME–AgNPs were comparatively highly efficient when compared to the other nanomaterials. This may be due to the fact that the presence of PDGF could enhance the antibacterial efficacy of *S. aureus*, which could be comparatively more efficient than EuME–AgNPs and EuME.[83] In addition, SBD–AgNPs was tested against *S. aureus*, and the zone of inhibition (mm) was 6 mm, which was not comparatively efficient when compared to PDGF/EuME–AgNPs as shown in Table S2. This shows that SBD–AgNPs were found to be significantly less efficient than PDGF/EuME–AgNPs. Therefore, the antibacterial activity of PDGF/EuME–AgNPs was comparatively more efficient than that of EuME, EuME–AgNPs and SBD–AgNPs.[84]

In treatment against *P. aeruginosa*, the uncapped AgNPs showed a minimum zone of inhibition of 5 mm, which was due to the uncapping properties of the silver nanomaterial. Chitosan:PVA showed a value of 2 mm, which was even less than that of uncapped AgNPs due to the absence of the core compound. Various concentrations of EuME (1%, 3%, 7%, and 9%) were treated against *P. aeruginosa*, and the zone of inhibition was 3 mm, 5 mm, 7 mm, and 8.5 mm as shown in Fig. S3(ii)(b). Inclusion of the eugenol compound in the eugenol composite material improved EuME's efficiency to a level comparable to that of uncapped AgNPs. Varying concentrations of EuME–AgNPs (1%, 3%, 7%, and 9%) were treated against *P. aeruginosa*, and the zone of inhibition (mm) was 4 mm, 9.5 mm, 14.5 mm and 17 mm, respectively, as shown in Fig. S3(ii)(c), which was comparatively greater than that of EuME. This may be due to the presence of a silver complex associated with the biopolymeric complex. PDGF was tested against *P. aeruginosa* at varying concentrations of 1%, 3%, 7%, and 9% and the zone of inhibition (mm) was 2 mm, 6 mm, 8 mm, and 9 mm, respectively, as shown in Fig. S3(ii)(d). Varying concentrations of PDGF/EuME–AgNPs (1%, 3%, 7%, and 9%) were tested, and the zone of inhibition (mm) was 10 mm, 19 mm, 21 mm, and 23 mm, respectively, as shown in Fig. S3(ii)(e), which shows that PDGF-impregnated EuME–AgNPs were comparatively highly efficient when compared to the other nanomaterials. This may be due to the presence of PDGF associated with the EuME–AgNPs, which show the highest antibacterial susceptibility when compared with EuME–AgNPs and EuME. In addition, SBD–AgNPs were tested against *P. aeruginosa*, and the zone of inhibition (mm) was 6 mm, which was comparatively less efficient than PDGF/EuME–AgNPs as shown in Table S2. This shows that SBD–AgNPs were found to be significantly less efficient than PDGF/EuME–AgNPs. Therefore, in comparison to EuME, EuME–AgNPs, and SBD–AgNPs, the antibacterial activity of PDGF/EuME–AgNPs was more effective against *P. aeruginosa*.[85]

### 3.5. Biosafety evaluation

**3.5.1. Determination of cell viability.** The viability of eugenol-based nanomaterials, namely, EuME, EuME–AgNPs, PDGF/EuME–AgNPs and SBD–AgNPs, was determined at varying concentrations of 20 μg $mL^{-1}$, 10 μg $mL^{-1}$, and 1 μg $mL^{-1}$. The percentage of viability of PDGF/EuME–AgNPs increases to 76.7% at 20 μg $mL^{-1}$ and upon decreasing the concentration to 10 μg $mL^{-1}$ and 1 μg $mL^{-1}$ the percentage of viability decreases to 69.1% and 58.9%, respectively. Similarly, the percentage of viability of EuME–AgNPs increases to 60.7% at 20 μg $mL^{-1}$ and upon decreasing the concentration to 10 μg $mL^{-1}$ and 1 μg $mL^{-1}$ the percentage of viability decreases to 53.2% and 45.7%, respectively. The percentage of viability of EuME increases to 52.8% at 20 μg $mL^{-1}$ and upon decreasing the concentration to 10 μg $mL^{-1}$ and 1 μg $mL^{-1}$ the percentage of viability decreases to 44.4% and 39.8%, respectively. The percentage of viability of SBD–AgNPs increases to 9.3% at 20 μg $mL^{-1}$ and upon decreasing the concentration to 10 μg $mL^{-1}$ and 1 μg $mL^{-1}$ the percentage of viability decreases to 6.3% and 3.3%, respectively, as shown in Fig. 4a.

An increase in concentration increases the percentage of viability in lymphocytes. The percentage of viability of PDGF/EuME–AgNPs at 20 μg $mL^{-1}$ was 76.7%, which was greater than that of the eugenol-based nanomaterials EuME, EuME–AgNPs, and SBD–AgNPs, for which the values were 52.8%, 60.7% and 9.3%, respectively. The percentage of viability of PDGF/EuME–AgNPs at 10 μg $mL^{-1}$ was 69.1%, which was greater than that of the eugenol-based nanomaterials EuME, EuME–AgNPs, and SBD–AgNPs, for which the values were 44.4%, 53.2% and 6.3%, respectively. The percentage of viability of PDGF/EuME–AgNPs at 1 μg $mL^{-1}$ was 58.9%, which was greater than that of the eugenol-based nanomaterials EuME, EuME–AgNPs, and SBD–AgNPs, for which the values were 39.8%, 45.7%, and 3.3%, respectively, as shown in Fig. 4a. Hence, the percentage of viability of the eugenol-based nanomaterials EuME, EuME–AgNPs, and PDGF/EuME–AgNPs was higher than that of SBD–AgNPs upon interaction with the lymphocytes. This may be due to the fact that eugenol-based growth factor impregnated nanofibrous mats contain phenylpropanoid compounds (allyl chain substituted hydroxyl groups), which could interact with the lymphocytes and be less cytotoxic to the biological system, thereby enhancing the percentage of cell viability when compared to SBD–AgNPs. Hence, eugenol-based nanomaterials

 

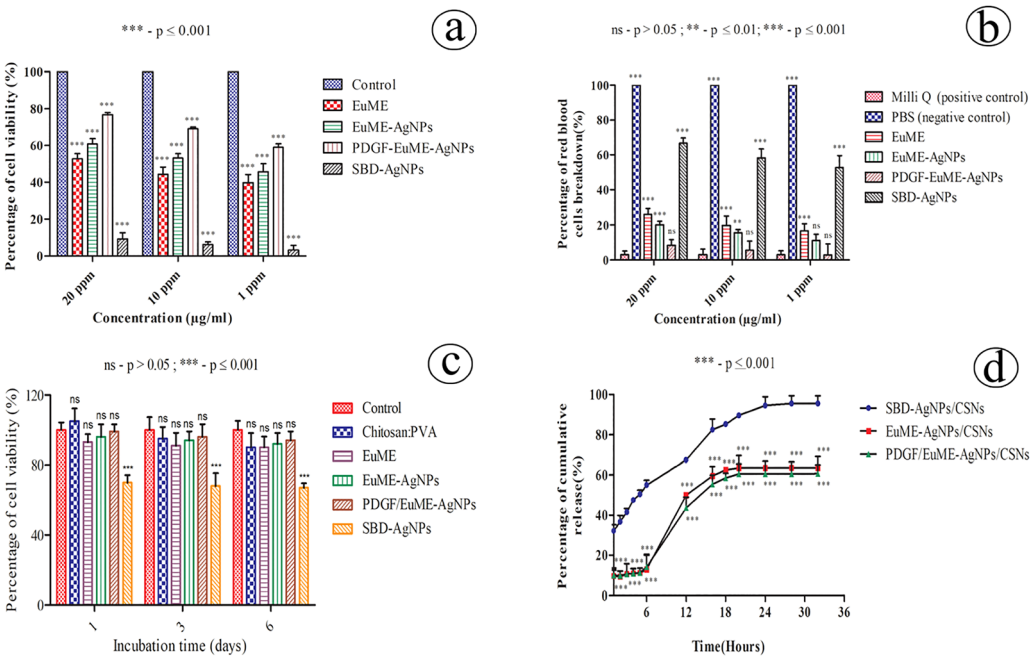


Fig. 4 (a) Determination of the cell viability (%) of silver nanomaterials interacting with white blood cells (human lymphocytes), (b) determination of the percentage of hemolysis (%) caused by silver nanomaterials interacting with red blood cells (human erythrocytes), (c) determination of cytotoxicity using 3T3 mouse fibroblast cell lines, (d) determination of silver ion release kinetics of eugenol microemulsion (EuME)-based silver core–sheath nanofibrous mats (CSNs).

were thermodynamically stable and possessed drug loading capacity, thus exhibiting antimicrobial and anti-inflammatory properties.[86] The statistical analysis showed that the viability of PDGF/EuME–AgNPs was significantly different from that of SBD–AgNPs but less significantly different from that of EuME and EuME–AgNPs. The results showed that SBD–AgNPs were cytotoxic to lymphocytes, thereby damaging the cell wall, affecting cell membrane integrity and reducing viability. Although EuME and EuME–AgNPs possess anti-inflammatory and antibacterial properties, PDGF/EuME–AgNPs possess the maximum healing and regenerative potential upon interaction with human lymphocytes, showing an increase in the percentage of cell viability.[87] Hence, the results clearly reveal that PDGF/EuME–AgNPs showing greater viability were more hemocompatible than SBD–AgNPs.

**3.5.2. Determination of cell hemolysis.** The hemolysis of the eugenol-based nanomaterials EuME, EuME–AgNPs, PDGF/EuME–AgNPs, and SBD–AgNPs was tested by interacting them with red blood cells (human erythrocytes) at different concentrations, namely 20 μg $mL^{-1}$, 10 μg $mL^{-1}$ and 1 μg $mL^{-1}$, as shown in Fig. 4b. The hemolysis (%) of PDGF/EuME–AgNPs at 20 μg $mL^{-1}$ was 8.33% and upon decreasing the concentration to 10 μg $mL^{-1}$ and 1 μg $mL^{-1}$, the hemolysis was 5.55% and 2.77%, respectively. Similarly, the hemolysis (%) of EuME at 20 μg $mL^{-1}$ was 26.11% and upon decreasing the concentration to 10 μg $mL^{-1}$ and 1 μg $mL^{-1}$, the hemolysis was 19.77% and 16.66%, respectively. The hemolysis (%) of EuME–AgNPs at 20 μg $mL^{-1}$ was 20% and upon decreasing the concentration to 10 μg $mL^{-1}$ and 1 μg $mL^{-1}$, the hemolysis was 15.44% and 11.11%, respectively. The hemolysis (%) of SBD–AgNPs at 20 μg $mL^{-1}$ was 66.66% and upon decreasing the concentration to 10 μg $mL^{-1}$ and 1 μg $mL^{-1}$, the hemolysis was 58.33% and 52.77%, respectively, as shown in Fig. 4b. Hence, a slight decrease in the concentration of the nanomaterial reduces the percentage of cell hemolysis. The percentage of cell hemolysis of PDGF/EuME–AgNPs at 20 μg $mL^{-1}$ was 8.33%, which was less than that of the eugenol-based nanomaterials EuME, EuME–AgNPs, and SBD–AgNPs, for which the values were 26.11%, 20%, and 66.66%, respectively. Similarly, the percentage of cell hemolysis of PDGF/EuME–AgNPs at 10 μg $mL^{-1}$ was 5.55%, which was less than that of the eugenol-based nanomaterials EuME, EuME–AgNPs, and SBD–AgNPs, for which the values were 19.77%, 15.44%, and 58.33%, respectively. The percentage of cell hemolysis of PDGF/EuME–AgNPs at 1 μg $mL^{-1}$ was 2.77%, which was less than that of the eugenol-based nanomaterials EuME, EuME–AgNPs, and SBD–AgNPs, for which the values were 16.66%, 11.11%, and 52.77%, respectively, as shown in Fig. 4b. Hence, the percentage of hemolysis of PDGF/EuME–AgNPs was statistically more significant than that of eugenol-based nanomaterials (EuME, EuME–AgNPs, and SBD–AgNPs).

Eugenol-based growth factor-impregnated nanomaterials contain phenolic compounds, namely flavonoids, which play a vital role in anti-inflammatory and angiogenic properties. Eugenol-impregnated nanomaterials were found to be less cytotoxic to the biological system and possess excellent hemocompatibility properties.[88] The statistical analysis showed that the hemolysis of PDGF/EuME–AgNPs was significantly different from that of SBD–AgNPs but less significantly different from that of EuME and EuME–AgNPs. SBD–AgNPs were found to be

cytotoxic to erythrocytes, thereby damaging the integrity of red blood cells and increasing hemolysis. Although EuME and EuME–AgNPs possess anti-inflammatory and angiogenic properties, PDGF/EuME–AgNPs possess the maximum wound healing potential upon interaction with human erythrocytes, showing a reduction in the percentage of cell hemolysis.[89] Hence, PDGF/EuME–AgNPs showing greater efficiency were comparatively more hemocompatible than SBD–AgNPs.

### 3.6. Determination of cytotoxicity

The percentage of cell viability of mouse fibroblast cell lines (3T3 fibroblast cells) was used to examine the cytotoxicity of the nanomaterials. The PDGF/EuME–AgNPs are considered for diabetic wound healing applications as well as skin tissue engineering. The fibroblast cells play a critical role in supporting wound healing processes, being involved in fragmenting fibrin clots, creating extracellular matrix components, and forming collagen structures to support the cells associated with efficient wound healing, wound contraction, and angiogenesis. Hence, we chose 3T3 fibroblast cell lines for the study. The fibroblast cells are mouse-derived and have a good proliferation rate. The percentage of cell viability using the MTT assay was determined by culturing and harvesting the fibroblast cells with the extraction media of the nanomaterials after three incubation intervals (1, 3, and 6 days), as shown in Fig. 4c.

The figure confirms that the percentage of cell viability of chitosan:PVA, EuME, EuME–AgNPs, and PDGF/EuME–AgNPs was found to be comparatively higher than that of SBD–AgNPs during the three consecutive incubation time intervals (1, 3, and 6 days). As per the statistical analysis, the percentage of cell viability does not show any significant changes in comparison to the control group. The experimental results confirmed that the nanomaterials showed no adverse cytotoxic effects upon interaction with 3T3 mouse fibroblast cells.

The percentage of cell viability of chitosan:PVA, EuME, EuME–AgNPs, and PDGF/EuME–AgNPs was found to be comparatively higher than that of SBD–AgNPs during the three consecutive incubation time intervals (1, 3, and 6 days). All the samples showed a greater percentage of cell viability above 90% in accordance with the control extraction medium. This may be due to the fact that nanomaterials showed no cytotoxic effects upon interaction with fibroblast cells, thereby promoting cell viability and cell proliferation. The PDGF/EuME–AgNPs possess the highest percentage of cell viability when compared with the other nanomaterials. This may be due to the fact that PDGF-BB enhances fibroblast growth and promotes fibrogenesis. Numerous studies have shown that PDGF-BB accelerates cell proliferation and migration under different pathological conditions and thus enhances tissue remodeling and wound healing in diabetic patients.[90] Hence, PDGF plays an important role in enhancing fibroblast growth and proliferation, which could be a crucial factor in diabetic wound healing.

### 3.7. Release kinetics

The growth factor-impregnated nanomaterials exhibit sustained dissolution behavior in wound healing applications. Electrospun nanofibrous mats offer major advantages due to their release and sorption properties. The important characteristics of nanofibrous mats, such as small pores and high surface area, are very favorable for liquid adsorption, sustained release, and protecting the target site from bacterial penetration, thus providing a suitable microenvironment for wound healing.[91] Although there are an enormous number of concepts in wound healing applications, the release kinetics of CSNs in simulated wound fluids remains unexplored. The study mainly focuses on the release kinetics of CSNs in SWF, which could be correlated with the toxicological behavior of nanomaterials. Fig. 4d shows the release kinetics of CSNs (PDGF/EuME–AgNPs/CSNs, EuME–AgNPs/CSNs, and SBD–AgNPs/CSNs).

The percentage of cumulative release of PDGF/EuME–AgNPs/CSNs at 1, 2, 3, 4, 5, 6, 12, 16, 18, 20, 24, 28 and 32 hours was measured to be 9.93%, 9.79%, 10.61%, 10.92%, 11.27%, 14.09%, 43.64%, 55.42%, 58.42%, 60.53%, 60.53%, 60.48% and 60.68%, respectively. The percentage of cumulative release of EuME–AgNPs/CSNs at 1, 2, 3, 4, 5, 6, 12, 16, 18, 20, 24, 28 and 32 hours was measured to be 9.61%, 9.33%, 10.61%, 10.87%, 11.10%, 12.87%, 49.83%, 59.42%, 62.42%, 63.42%, 63.42%, 63.54% and 63.42%, respectively. The percentage of cumulative release of SBD–AgNPs/CSNs at 1, 2, 3, 4, 5, 6, 12, 16, 18, 20, 24, 28 and 32 hours was measured to be 32.11%, 36.65%, 41.43%, 47.42%, 50.34%, 54.98%, 67.36%, 82.43%, 85.18%, 89.54%, 96.54%, 97.47% and 97.53%, respectively. Fig. 4d shows that the percentage of release of PDGF/EuME–AgNPs/CSNs that exhibit sustained dissolution behavior was approximately 60.68% during the 32nd hour, whereas that of SBD–AgNPs/CSNs was approximately more than 97.53%, which was observed to be a sudden release of silver ions in the simulated wound fluid system. Particularly, during the period of 12–32 hours, PDGF/EuME–AgNPs/CSNs and EuME–AgNPs/CSNs exhibited a more controlled release of approximately 60.68% and 63.42% when compared to SBD–AgNPs/CSNs, which exhibited a sudden release of silver ions in the simulated wound fluid system. Due to impregnation of the growth factor, PDGF/EuME–AgNPs/CSNs exhibit a progressive change during the 12th–20th hour, which may be due to the shift in the systemic release of the bioactive compounds present in the fabricated nanofibrous mats when compared to EuME–AgNPs/CSNs. The release of SBD–AgNPs/CSNs resulted in sudden metallic ion release, which may be due to the fact that SBD–AgNPs/CSNs consist of aggregated metallic silver ions, which interfere with the dissolution kinetics behavior. The release of eugenol-based nanomaterials resulted in a sustained and controlled release of metallic ions coupled with biopolymeric chains showing less cytotoxicity to living cells. The duration of release studies was rationally selected ranging from 0 to 32 hours. This is to mimic the scenario that the initial 2 days post injury are considered very crucial in the wound healing process. The PDGF impregnated EuME–AgNPs/CSNs exhibit a sustained gradual release, while the growth factor uncoated nanofibrous mats exhibit a sudden release in the SWF system. In addition, the emulsion containing the silver nanocomposites was found to be stable for more than 48 hours, and hence

 

the duration of 32 hours for the release kinetics study is appropriate. Also, the respective study timeline helps understand the interaction of growth factor impregnated nanocomposites in the real diabetic wound healing scenario. The statistical analysis shows that PDGF/EuME–AgNPs/CSNs and EuME–AgNPs/CSNs possess a greater significant difference (***) ($p$ value $\leq$ 0.001) than SBD–AgNPs/CSNs. This may be due to the sustained dissolution behavior of eugenol-based metallic silver ions in the wound environment. According to the literature, the dissolution behavior of nanomaterials depends on the bioactive components and metallic ions present in the core–sheath nanofibrous material.[92] Hence, eugenol-based nanomaterials such as PDGF/EuME–AgNPs/CSNs and EuME–AgNPs/CSNs exhibit sustained release kinetics due to the presence of flavonoids in the CSNs.

### 3.8. *In vivo* diabetic wound healing efficacy

**3.8.1. Percentage of wound contraction.** Wound healing in diabetes is impaired by factors that are both intrinsic and extrinsic to the wounds and their biological implications. Diabetic wound sites create a breeding ground for many resistant bacteria due to decreased neovascularization and re-epithelialization, accelerated high glucose levels, and a destructive wound healing response.[93] Nanofiber-based wound dressing models protect the wound bed from risk factors and provide a suitable microenvironment for facilitating the wound healing cascade. The porous structure and large surface area of CSNs facilitate the release of various bioactive molecules and mimic the innate extracellular matrix (ECM), which creates a suitable environment for cell proliferation, migration, and differentiation.[94] The rate at which bioactive molecules are released from wound dressing models can be effectively controlled by modifying the size and structure of the nanofiber pores, thereby promoting the wound healing process. Therefore, co-axial electrospun nanofibers are regarded as a great alternative to diabetic wound healing treatment in view of their exclusive benefits.

An *in vivo* diabetic wound healing study of the fabricated CSNs was performed using an excision wound model made with a thickness of 2 cm $\times$ 2 cm in STZ-induced diabetic rats. The fabricated CSNs were topically placed on the excisional wound sites, and the percentage of wound contraction was calculated at different time intervals. To assess the effectiveness of the CSNs to treat diabetic wounds, the wound area was imaged on days 0, 3, 6, 9, 14, and 25.

Fig. 5 and Fig. S5 determine the diabetic wound healing efficiency of the control group (no treatment), vehicle control (citrate buffer), chitosan:PVA/CSNs, EuME/CSNs, EuME–AgNPs/CSNs, PDGF/CSNs, PDGF/EuME–AgNPs/CSNs, and SBD–AgNPs/CSNs in STZ-induced diabetic rats. As shown in Fig. 5, diabetic wounds treated with PDGF/EuME–AgNPs/CSNs showed a greater percentage of wound contraction on the 9th day itself when compared to the control group (no treatment), vehicle control (citrate buffer), chitosan:PVA/CSNs, EuME/CSNs, EuME–AgNPs/CSNs, PDGF/CSNs, and SBD–AgNPs/CSNs. As shown in Fig. S5, the percentage of wound contraction and *in vivo* diabetic wound healing efficacy in STZ-induced diabetic rats were determined. From Fig. S5, on the 3rd day, the percentage of wound contraction in the control group (no treatment), vehicle control (citrate buffer), chitosan:PVA/CSNs, EuME/CSNs, EuME–AgNPs/CSNs, PDGF/CSNs, PDGF/EuME–AgNPs/CSNs, and SBD–AgNPs/CSNs was found to be 5%, 11.17%, 20.35%, 25.62%, 30%, 10.73%, 49%, and 15.36%, respectively. Similarly, on the 6th day, the percentage of wound contraction in the control group (no treatment), vehicle control (citrate buffer), chitosan:PVA/CSNs, EuME/CSNs, EuME–AgNPs/CSNs, PDGF/CSNs, PDGF/EuME–AgNPs/CSNs, and SBD–AgNPs/CSNs was found to be 15%, 30.8%, 54.95%, 61%, 71.87%, 40.52%, 90.62%, and 25.75%, respectively. On the 9th day, the percentage of wound contraction in the control group (no treatment), vehicle control (citrate buffer), chitosan:PVA/CSNs, EuME/CSNs, EuME–AgNPs/CSNs, PDGF/CSNs, PDGF/EuME–AgNPs/CSNs, and SBD–AgNPs/CSNs was found to be 20%, 80%, 82%, 91%, 93%, 70.55%, 98%, and 40%, respectively. On the 14th day, the percentage of wound contraction in the control group (no treatment), vehicle control (citrate buffer), chitosan:PVA/CSNs, EuME/CSNs, EuME–AgNPs/CSNs, PDGF/CSNs, PDGF/EuME–AgNPs/CSNs, and SBD–AgNPs/CSNs was found to be 25%, 82.12%, 96.25%, 97%, 98%, 85.37%, 100%, and 61%, respectively. On the 25th day, the percentage of wound contraction in the control group (no treatment), vehicle control (citrate buffer), chitosan:PVA/CSNs, EuME/CSNs, EuME–AgNPs/CSNs, PDGF/CSNs, PDGF/EuME–AgNPs/CSNs, and SBD–AgNPs/CSNs was found to be 40%, 91.25%, 98%, 100%, 100%, 92.12%, 100%, and 91%, respectively. Similarly, on the 30th day, the percentage of wound contraction in the control group (no treatment), vehicle control (citrate buffer), chitosan:PVA/CSNs, EuME/CSNs, EuME–AgNPs/CSNs, PDGF/CSNs, PDGF/EuME–AgNPs/CSNs, and SBD–AgNPs/CSNs was found to be 51%, 100%, 100%, 100%, 100%, 100%, 100%, and 95%, respectively. Although the efficiency of chitosan:PVA/CSNs, EuME/CSNs, EuME–AgNPs/CSNs, PDGF/CSNs, and SBD–AgNPs/CSNs was greater than that of the control group, PDGF/EuME–AgNPs/CSNs exhibited the highest percentage of wound contraction. The efficiency of PDGF/EuME–AgNPs/CSNs may be due to the impregnation of the growth factor along with EuME–AgNPs coupled with the biopolymeric matrix. The diabetic wounds treated with the PDGF-associated eugenol-based nanofibrous matrix exhibit a marked increase in the number of inflammatory cells that enter the wound, which include monocytes, neutrophils, and fibroblasts. Subsequently, the formation of granulation tissue was also enhanced. In addition, the PDGF-associated nanofibrous matrix promotes neovascularization and re-epithelialization potential. According to the statistical findings, the PDGF/EuME–AgNPs/CSNs group was observed to be substantially different from the control (without treatment) group. The experimental results of PDGF/EuME–AgNPs/CSNs were consistent with other research findings.[95] The percentage of wound contraction of EuME–AgNPs/CSNs was greater than that of EuME/CSNs, chitosan:PVA/CSNs, SBD–AgNPs/CSNs, and the control group on all the respective days (3, 6, 9, 14, 25, and 30), which may be due to the presence of an eugenol-based silver complex associated with the biopolymeric matrix. The eugenol-based silver nanocomposite

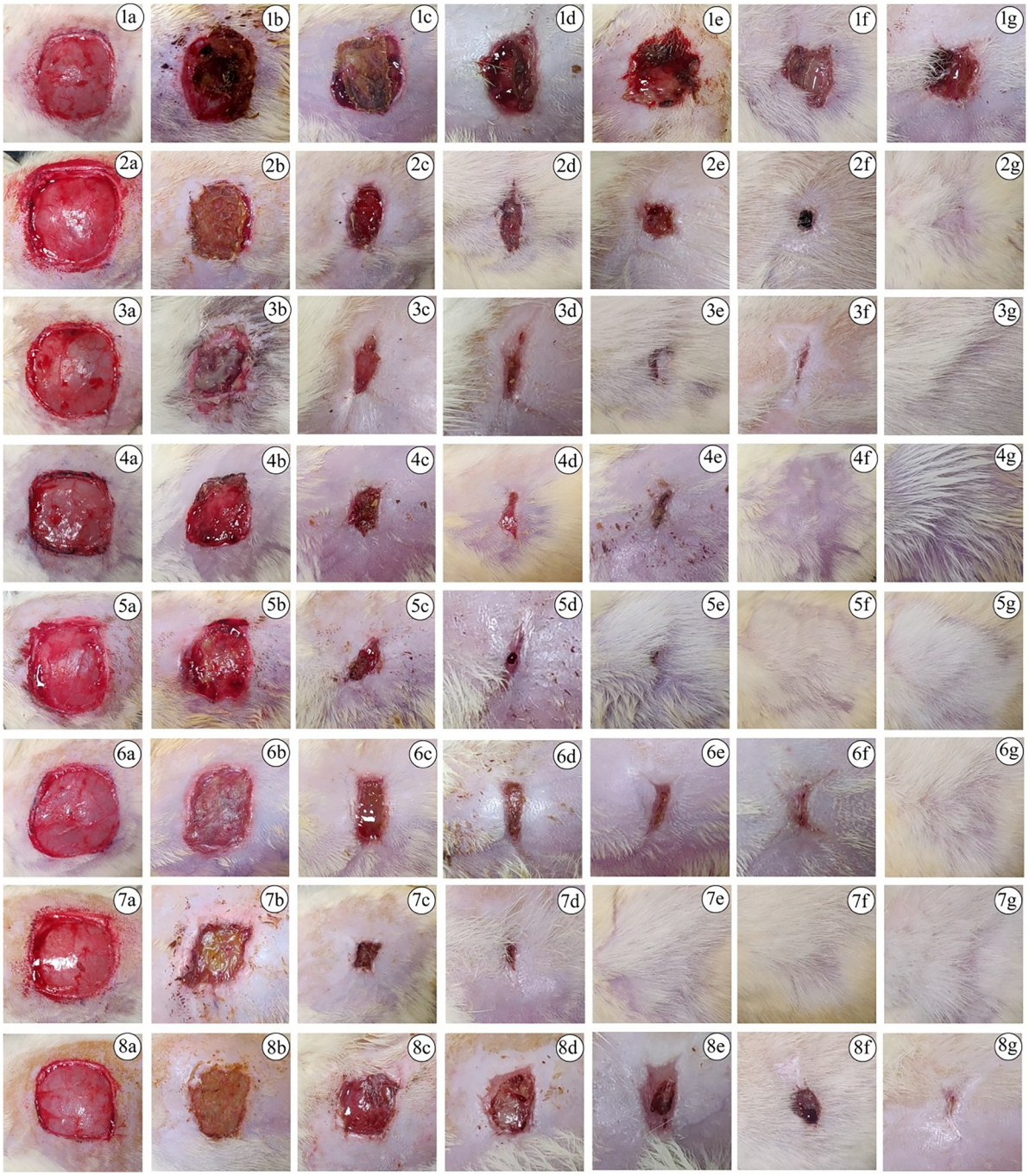


Fig. 5 Determination of the diabetic wound healing efficiency of core–sheath nanofibrous mats (CSNs) in streptozotocin (STZ) induced Wistar rat models with respect to time duration (days). (a) Excision wound healing during the 0th day, (b) excision wound healing during the 3rd day, (c) excision wound healing during the 6th day, (d) excision wound healing during the 9th day, (e) excision wound healing during the 14th day, (f) excision wound healing during the 25th day, and (g) excision wound healing during the 30th day; (1a–1g) control group (without treatment), (2a–2g) vehicle control (citrate buffer), (3a–3g) chitosan:PVA/CSNs, (4a–4g) EuME/CSNs, (5a–5g) EuME–AgNPs/CSNs, (6a–6g) PDGF/CSNs, (7a–7g) PDGF/EuME–AgNPs/CSNs, and (8a–8g) SBD–AgNPs/CSNs.

fibrous matrix heals the diabetic wound bed faster and protects the wound from biofilm formation. This could eventually accelerate wound closure and contraction and speed up the diabetic wound healing cascade. According to the statistical findings, EuME–AgNPs/CSNs were found to be significantly different ($p \leq 0.001$) from the control group. The experimental findings of EuME–AgNPs/CSNs turned out to be in line with the results of other studies.[96] The percentage of wound contraction of EuME/CSNs was greater than that of chitosan:PVA/CSNs, SBD–AgNPs/CSNs, and the control group on all the respective days (3, 6, 9, 14, 25, and 30). This may be due to the presence of flavonoids, a type of phenolic molecule that plays a crucial role

in the healing process by accelerating the cascade of wound contraction. According to the statistical findings, EuME/CSNs were found to be significantly different ($p \leq 0.001$) from the control group. The experimental findings of EuME/CSNs turned out to be analogous to those from other studies.[97] The percentage of wound contraction of chitosan:PVA/CSNs was greater than that of SBD–AgNPs/CSNs and the control group on all respective days (3, 6, 9, 14, 25, and 30), which may be due to the presence of a potent healing agent, such as chitosan, that plays a vital role in skin lesions and is effectively used as a wound dressing model. According to the statistical findings, chitosan:PVA/CSNs were found to be substantially different ($p \leq 0.001$) from the control group. The experimental findings of chitosan:PVA/CSNs were consistent with those of other studies.[98] The percentage of wound contraction of SBD–AgNPs/CSNs was found to be significantly less than that of chitosan:PVA/CSNs, EuME/CSNs, EuME–AgNPs/CSNs, PDGF/CSNs, and PDGF/EuME–AgNPs/CSNs, which may be due to the cytotoxic behavior of the polyamides present in the silver band aid suspension, which leads to decreased efficiency of the healing process in diabetic wounds. The statistical observations reveal that SBD–AgNPs/CSNs were found to be less significantly different ($p \leq 0.5$) from the control group and more significantly different ($p \leq 0.001$) from chitosan:PVA/CSNs, EuME/CSNs, EuME–AgNPs/CSNs, PDGF/CSNs, and PDGF/EuME–AgNPs/CSNs. Hence, the *in vivo* experimental results prove that PDGF/EuME–AgNPs/CSNs were found to be considerably more efficient than chitosan:PVA/CSNs, EuME/CSNs, EuME–AgNPs/CSNs, PDGF/CSNs, SBD–AgNPs/CSNs, and the control group.

**3.8.2. Estimation of blood glucose levels during the healing process.** The level of blood glucose was estimated on post-wounded days 0, 20, and 30 days in STZ-induced Wistar rats, as shown in Table S3. The measurement of blood glucose levels during the wound healing process is very essential. From Table S3, it can be observed that the treatment of diabetic rats with chitosan:PVA/CSNs resulted in a decrease in the blood glucose level, which may be due to the multifunctional characteristics of chitosan. Chitosan plays a crucial role in reducing oxidative stress and systemic inflammation, eventually neutralizing ROS production and thereby inhibiting glucose absorption. In addition, the nanofibrous mats impregnated with chitosan:PVA exhibit a sustained release of bioactive components, which in turn also supports glycemic stability in rats.[99] Rats treated with EuME/CSNs maintained steady glycemic levels without any increase in blood glucose, which favors a suitable microenvironment for efficient diabetic wound healing.

Rats treated with EuME–AgNPs/CSNs resulted in a decrease in blood glucose levels, which may be due to the presence of a silver nanocomposite matrix coupled with a biopolymer that enhanced the percentage of wound contraction, thereby reducing blood glucose levels in diabetic rats. Rats treated with PDGF/EuME–AgNPs/CSNs showed a reduction in blood glucose levels, which may be due to the impregnation of growth factors associated with the eugenol-based biopolymeric matrix. Growth factors are regarded as polypeptides that exert cellular functions resulting in cell proliferation, migration, and differentiation. Growth factors such as platelet-derived growth factor (PDGF) play a vital role in diabetic wound healing and could regulate cell growth and division. Hence, PDGF/EuME–AgNPs/CSNs resulted in a decrease in glycemic levels due to the impregnation of the growth factor-associated eugenol-based biopolymeric matrix. Diabetic rats treated with SBD–AgNPs/CSNs (commercially procured bandages) maintained a steady blood glucose level in the range of (400–450) mg $dL^{-1}$ without any increase in hyperglycemia, which resulted in nearly 80% of wound contraction on the 25th day of wound treatment. But the diabetic rats in the control group (without treatment) exhibited an increase in the blood glucose level, which may be due to the fact that no treatment has been administered to diabetic rats, which could have resulted in increased biofilm formation and delayed wound closure and contraction. Therefore, treatment groups with biopolymer-based nanofibrous mats maintained a steady, and at times decreased, blood glucose level, which could be an added value for diabetic wound healing applications.

**3.8.3. Histopathological study.** Histopathological analysis of STZ-induced diabetic excisional wound rat models in the control group (without treatment), vehicle control (citrate buffer), chitosan:PVA/CSNs, EuME/CSNs, EuME–AgNPs/CSNs, PDGF/CSNs, PDGF/EuME–AgNPs/CSNs, and SBD–AgNPs/CSNs observed on the 9th and 14th days was conducted using H&E staining (Fig. 6) and MT staining (Fig. 7). Table S4 presents the collagen and fibroblast regeneration potential.

As shown in Fig. 6, on the 9th day, using H&E staining, wounds treated as the control group showed mild atrophy of the epidermis and slightly dispersed collagen fibers in the dermis (Fig. 6.1(a)). Wounds treated as the vehicle control (citrate buffer) showed a normal epidermis (yellow arrow), the dermis showed mild edema, and scattered chronic inflammatory cells (black arrow) were observed (Fig. 6.1(b)). Wounds treated with chitosan:PVA/CSNs showed a normal-appearing epidermis (yellow arrow), the dermis showed mild edema, and scattered chronic inflammatory cells with normally dispersed collagen fibers (black arrow) were observed (Fig. 6.1(c)). Wounds treated with EuME/CSNs showed dense formation of the normal epidermis (yellow arrow), and the dermis showed few scattered chronic inflammatory cells with a high amount of collagen fiber formation (black arrow) (Fig. 6.1(d)) Wounds treated with EuME–AgNPs/CSNs showed a highly developed epidermis (yellow arrow), and the dermis showed maximum formation of collagen and fibroblasts (black arrow) in the treated groups (Fig. 6.1(e)). Wounds treated with PDGF/CSNs showed hyperplastic epidermal layers with a thin keratin layer (yellow arrow), and the dermis showed granulation tissue composed of hemorrhagic areas with fibroblast proliferation and increased fibrin regeneration (black arrow) (Fig. 6.1(f)). Wounds treated with PDGF/EuME–AgNPs/CSNs showed focal hyperplasia of the epidermis (yellow arrow) and the dermal layer expressed increased production of collagen fibers and fibroblast regeneration in the treated groups (Fig. 6.1(g)). Wounds treated with SBD–AgNPs/CSNs showed a normal epidermis (yellow arrow) and the dermis showed mild edema (black arrow) with little formation of collagen and fibroblasts

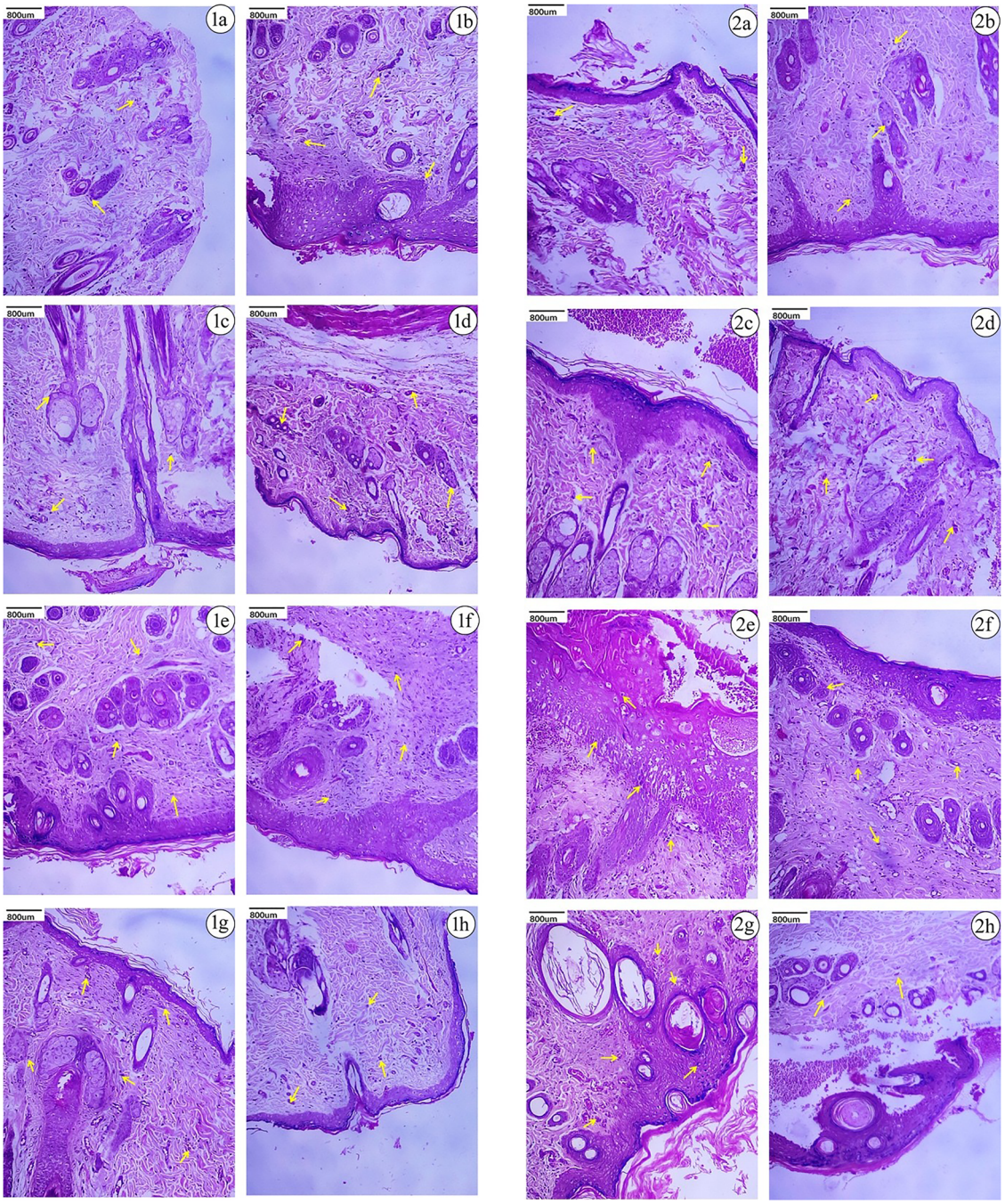


Fig. 6 Histopathological observations of wounds treated with core–sheath nanofibrous mats (CSNs) using hematoxylin and eosin (H&E) staining on the 9th and 14th days. (1a–1h) Skin sections stained on the 9th day of wound closure, (2a–2h) skin sections stained on the 14th day of wound closure, (1a and 2a) control group (without treatment), (1b and 2b) vehicle control (citrate buffer), (1c and 2c) chitosan:PVA/CSNs, (1d and 2d) EuME/CSNs, (1e and 2e) EuME–AgNPs/CSNs, (1f and 2f) PDGF/CSNs, (1g and 2g) PDGF/EuME–AgNPs/CSNs, and (1h and 2h) SBD–AgNPs/CSNs. The yellow arrow indicates the production of fibroblasts, collagen deposition, and granulation tissue formation in the stained skin sections on the 9th and 14th days.

in the treated groups (Fig. 6.1(h)). The observed results showed that, on the 9th day, wounds treated with PDGF/EuME–AgNPs/CSNs showed the maximum formation of collagen and fibroblasts and fibrin regeneration when compared to the other treatment groups.

As shown in Fig. 6, on the 14th day, using H&E staining, wounds treated as the control group showed a hyperplastic epidermis (regenerative changes) (yellow arrow), and the dermis showed granulation tissue composed of chronic inflammatory cells (black arrow) (Fig. 6.2(a)). Wounds treated as the vehicle control (citrate buffer) showed an atrophied epidermis (yellow arrow) and normal dermal layers with mild edema (black arrow) (Fig. 6.2(b)). Wounds treated with chitosan:PVA/CSNs showed mild atrophy of the epidermis (yellow arrow), and

the maximum amount of fibroblasts was observed in the dermis layer (black arrow) (Fig. 6.2(c)). Wounds treated with EuME/CSNs showed an atrophied epidermis (yellow arrow) and maximum formation of collagen and fibroblasts in the dermal layer (black arrow) (Fig. 6.2(d)). Wounds treated with EuME–AgNPs/CSNs showed regenerative epidermal layers (yellow arrow) with spongiosis, and the dermis showed prominent granulation tissue composed of newly formed blood vessels, hemorrhagic areas, orderly proliferation of fibroblasts, and inflammation (black arrow) (Fig. 6.2(e)). Wounds treated with PDGF/CSNs showed a hyperplastic epidermis (yellow arrow) and normal dermal layers with organized collagen bundles (black arrow) (Fig. 6.2(f)). Wounds treated with PDGF/EuME–AgNPs/CSNs showed a normal epidermis with focal hyperplasia (yellow arrow) and a dermal layer with maximum production of fibroblasts and collagen and fibrin regeneration (Fig. 6.2(g)). Wounds treated with SBD–AgNPs/CSNs showed an atrophied epidermis (yellow arrow), and the dermis showed edema with a disordered collagen pattern and scattered inflammatory cells (black arrow) (Fig. 6.2(h)). The observed results show that on the 14th day, wounds treated with PDGF/EuME–AgNPs/CSNs showed the maximum amount of granulation tissue formation, and the dermis showed a dense formation of fibroblasts and collagen regeneration when compared to the other treatment groups.

As shown in Fig. 7, on the 9th day using MT staining, wounds treated as the control group showed normal deposition of collagen bundles, as shown in Fig. 7.1(a). Wounds treated as the vehicle control showed a disorganized distribution of collagen fibers, as shown in Fig. 7.1(b). Wounds treated with chitosan:PVA/CSNs exhibited an organized arrangement of normal collagen fibers, resulting in the complete formation of fibrin and fibroblast cells and tissues as shown in Fig. 7.1(c). Similarly, wounds treated with EuME/CSNs and EuME–AgNPs/CSNs showed equal distribution and arrangement of collagen fibers, and bundle-shaped patterns were observed, as shown in Fig. 7.1(d) and (e). Wounds treated with PDGF/CSNs and PDGF/EuME–AgNPs/CSNs showed an abundant number of organized collagen fibers and fibroblast proliferation, as shown in Fig. 7.1(f) and (g). Wounds treated with SBD–AgNPs/CSNs showed a disorganized distribution of collagen fibers, and irregular bundle-shaped patterns were observed, as shown in Fig. 7.1(h). The observed results show that wounds treated with PDGF/EuME–AgNPs/CSNs showed maximum production of collagen fibers and bundle-shaped regular patterns when compared to the other treatment groups. As shown in Fig. 7, on the 14th day using MT staining, wounds treated as the control group showed increased collagen fibers in a mildly disorganized pattern and fibroblast proliferation as shown in Fig. 7.2(a). Wounds treated as the vehicle control showed an organized distribution of collagen fibers (Fig. 7.2(b)). Wounds treated with chitosan:PVA/CSNs exhibited an equal and organized distribution of collagen fibers (Fig. 7.2(c)). Wounds treated with EuME/CSNs exhibited abundant formation of collagen proliferation in an organized manner and a bundle-shaped pattern as shown in Fig. 7.2(d). Wounds treated with EuME–AgNPs/CSNs exhibited abundant collagen proliferation in an organized pattern (Fig. 7.2(e)). Wounds treated with PDGF/CSNs exhibited the formation of normal collagen fibers in an organized pattern (Fig. 7.2(f)). Wounds treated with PDGF/EuME–AgNPs/CSNs showed abundant formation of collagen fibers, and the maximum amount of fibrin regeneration was observed (Fig. 7.2(g)). Wounds treated with SBD–AgNPs/CSNs exhibited mild collagen proliferation and a disorganized pattern of collagen fibers (Fig. 7.2(h)). The observed results prove that wounds treated with PDGF/EuME–AgNPs/CSNs showed maximum proliferation of collagen fibers and deposition when compared to the other treatment groups.

**3.8.4. Immunohistochemical study.** Angiogenesis plays a crucial role in the wound healing cascade. Angiogenesis enhances the transport of oxygen and nutrients to the injury sites. CD-31 is one of the most important markers of endothelial cell differentiation, which aids in proliferation, adhesion, and vascularization. CD-31 is expressed by monocytes, platelets, endothelial cells, and granulocytes.[100] Additionally, CD-31 plays a vital role in cellular migration and the removal of aged neutrophils in an inflammatory phase.

As shown in Fig. 8(a and b), immunohistochemical staining has been carried out using CD-31 as the marker for the treatment groups.

As shown in Fig. 8, wounds treated as the control group showed CD-31 mild focal positive staining in the dermis (yellow arrow) and no significant angiogenesis was observed (Fig. 8(1a and b)), whereas wounds treated with the vehicle control, chitosan:PVA/CSNs, EuME/CSNs, EuME–AgNPs/CSNs, PDGF/CSNs, and PDGF/EuME–AgNPs/CSNs exhibited an increased CD-31-stained area in the dermis layer (yellow arrow), which confirms vascularization potential in the respective groups. Significant amounts of angiogenesis are observed in the respective vehicle controls (Fig. 8(2a and b)), chitosan: PVA/CSNs (Fig. 8(3a and b)), EuME/CSNs (Fig. 8(4a and b)), EuME–AgNPs/CSNs (Fig. 8(5a and b)), PDGF/CSNs (Fig. 8(6a and b)) and PDGF/EuME–AgNPs/CSNs (Fig. 8(7a and b)). But wounds treated with SBD–AgNPs/CSNs showed a moderate amount of stained area in the dermis layer (yellow arrow), and little amount of angiogenesis was observed, as shown in Fig. 8(8a and b). Hence, the observed results reveal that wounds treated with eugenol-based nanofibrous mats showed an increased CD-31-stained section and a significant amount of angiogenesis when compared to the control group and SBD–AgNPs/CSNs.

IL-1 is a pro-inflammatory cytokine and possesses immune-amplifying effects. IL-1 is predominantly produced by macrophages and epithelial cells.[101] IL-1 plays a vital role in acute inflammation, which results in adaptive anti-tumor responses. As shown in Fig. 8(c and d), immunohistochemical staining has been carried out using IL-1 as the potential marker for the treatment groups. As shown in Fig. 8, wounds treated as the control group (Fig. 8(1c and d)) and the vehicle control group (Fig. 8(2c and d)) showed mild focal positivity for IL-1 in the inflammatory cells in the dermis (yellow arrow). No significant inflammation is observed similar to the control groups. Wounds treated with chitosan:PVA/CSNs (Fig. 8(3c and d))

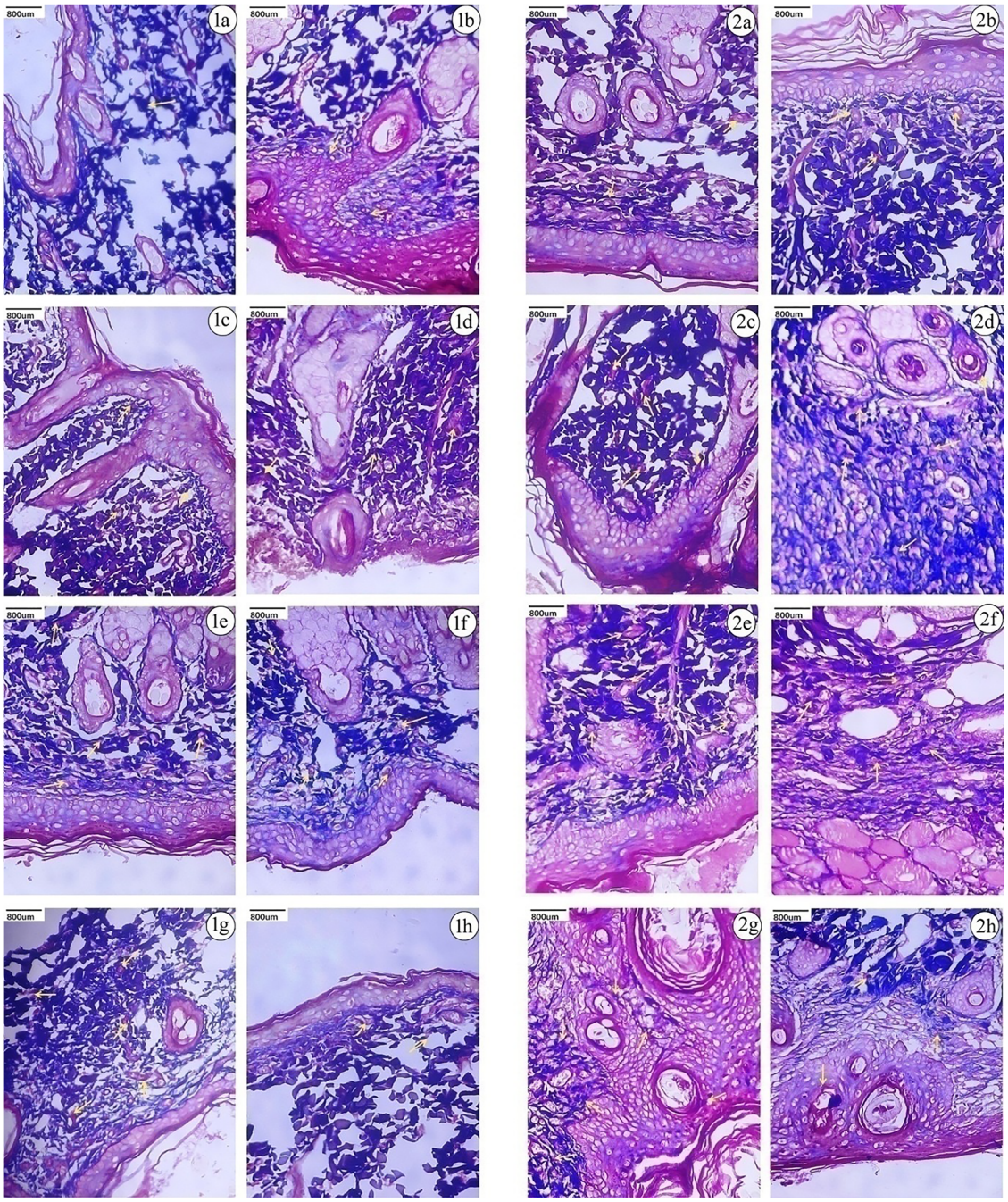


Fig. 7 Histopathological observations of wounds treated with core–sheath nanofibrous mats (CSNs) using Masson's trichrome (MT) staining on the 9th and 14th days. (1a–1h) Skin sections stained on the 9th day of wound closure, (2a–2h) skin sections stained on the 14th day of wound closure, (1a and 2a) control group (without treatment), (1b and 2b) vehicle control (citrate buffer), (1c and 2c) chitosan:PVA/CSNs, (1d and 2d) EuME/CSNs, (1e and 2e) EuME–AgNPs/CSNs, (1f and 2f) PDGF/CSNs, (1g and 2g) PDGF/EuME–AgNPs/CSNs, and (1h and 2h) SBD–AgNPs/CSNs. The yellow arrow denotes the quantitative determination of collagen deposition in the stained skin sections on the 9th and 14th days.

showed an increase in IL-1 positivity among the inflammatory cells (yellow arrow). A mild increase in the inflammatory cells was observed, as shown in the figure. Similarly, wounds treated with EuME/CSNs (Fig. 8(4c and d)), EuME–AgNPs/CSNs (Fig. 8(5c and d)), PDGF/CSNs (Fig. 8(6c and d)), and PDGF/EuME–AgNPs/CSNs (Fig. 8(7c and d)) showed an increase in IL-1 positivity among the inflammatory cells (yellow arrow). In addition, a significant increase in inflammatory cells was observed, as shown in the figure. But wounds treated with SBD–AgNPs/CSNs (Fig. 8(8c and d)) showed an increase in IL-1 positivity among the inflammatory cells (yellow arrow). Also, a mild increase in the inflammatory cells is observed, as shown in the figure. Hence, the observed results prove that wounds treated with PDGF/EuME–AgNPs/CSNs possess a high amount

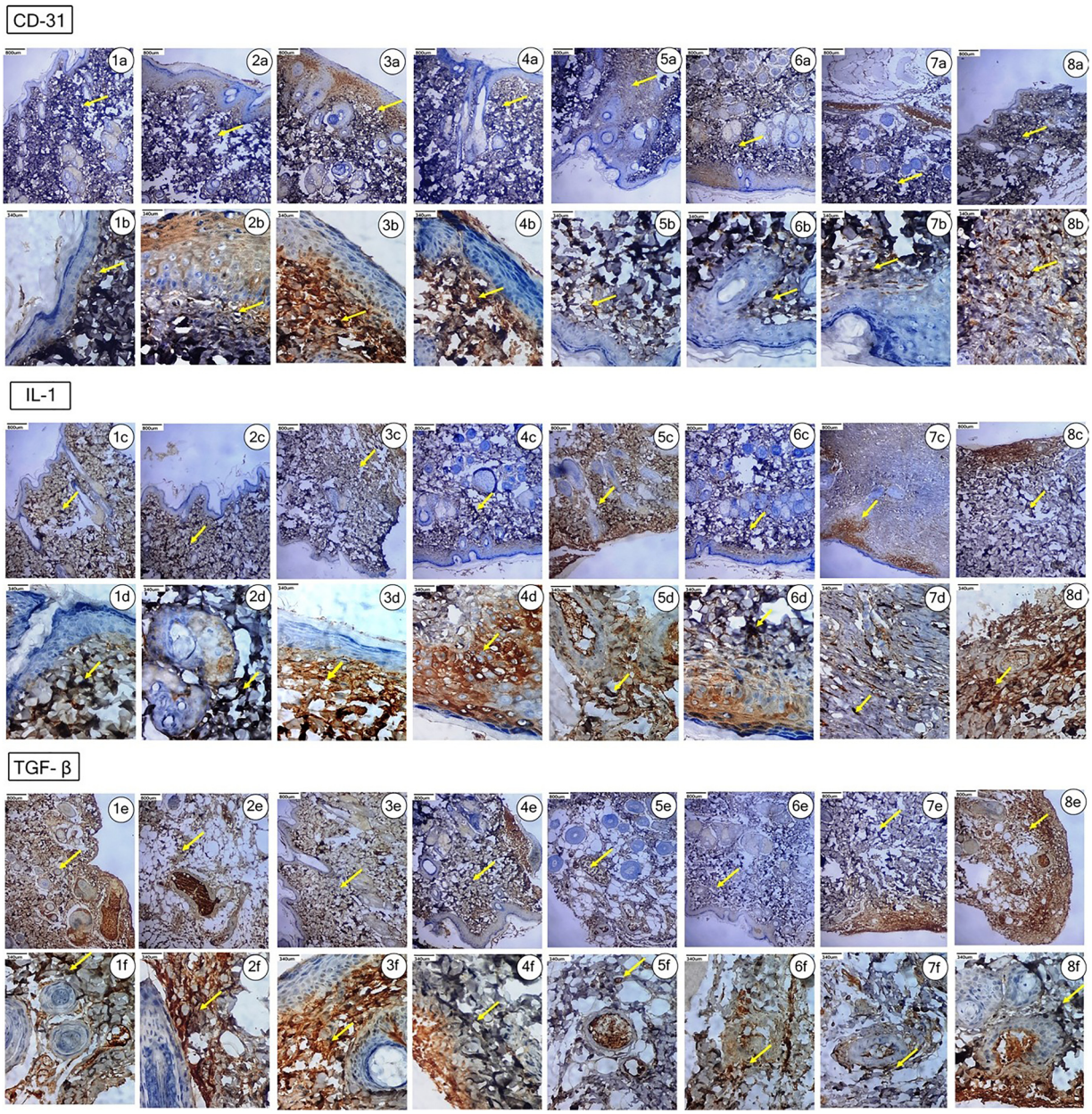


Fig. 8 Immunohistochemical study of wounds treated with core–sheath nanofibrous mats (CSNs) using potential anti-inflammatory markers such as CD-31, IL-1 and TGF-β during the diabetic wound healing process in streptozotocin (STZ) induced Wistar rat models. (1a–1f) Control group (without treatment), (2a–2f) vehicle control (citrate buffer), (3a–3f) chitosan:PVA/CSNs, (4a–4f) EuME/CSNs, (5a–5f) EuME–AgNPs/CSNs, (6a–6f) PDGF/CSNs, (7a–7f) PDGF/EuME–AgNPs/CSNs, and (8a–8f) SBD–AgNPs/CSNs. The yellow arrow indicates the determination of fibrogenesis and angiogenesis in the stained skin sections during the diabetic wound healing process using potential anti-inflammatory markers.

of IL-1 positivity among the inflammatory cells, and a significant increase in the inflammatory cells is observed when compared to the other treatment groups.

TGF-β is a potential marker in the replenishment and retrieval of immune cells and fibroblasts from circulation. These mechanistic events lead to the formation of granulation tissue, angiogenesis, and collagen synthesis and production.[102] As shown in Fig. 8(e and f), immunohistochemical staining has been carried out using TGF-β as the potential anti-inflammatory marker for the treatment groups. As shown in Fig. 8, wounds treated as the control group showed mild TGF-β1 positivity in the dermis layer (yellow arrow). No significant fibrogenesis was observed (Fig. 8(1e and f)). Wounds treated with the vehicle control, chitosan:PVA/CSNs, EuME/CSNs, EuME–AgNPs/CSNs, PDGF/CSNs, PDGF/EuME–AgNPs/CSNs, and SBD–AgNPs/CSNs exhibited accelerated TGF-β1 positivity in the dermis layer (yellow arrow). Significant fibrogenesis is observed as in the respective vehicle control (Fig. 8(2e and f)), chitosan:PVA/CSNs (Fig. 8(3e and f)), EuME/CSNs (Fig. 8(4e and f)), EuME–AgNPs/CSNs (Fig. 8(5e and f)), PDGF/CSNs (Fig. 8(6e and f)),

PDGF/EuME–AgNPs/CSNs (Fig. 8(7e and f)), and SBD–AgNPs/CSNs (Fig. 8(8e and f)). Hence, the observed results confirm that wounds treated with PDGF/EuME–AgNPs/CSNs exhibited the maximum amount of TGF-β1 positivity and a significant increase in fibrogenesis is observed when compared to the other treatment groups.

## 4. Conclusion

Multifunctional PDGF-impregnated eugenol-based CSNs (PDGF/EuME–AgNPs/CSNs) were efficiently fabricated. The CSNs determined the essential physico-chemical characteristics that were found to be major pre-requisites for diabetic wound healing applications. The surface morphology and internal morphology of PDGF/EuME–AgNPs/CSNs nanofibrous mats demonstrated smooth, bead-free, and web-like nanofibrous structures with a nanometer size range. The fabricated nanofibrous mats showed good water uptake, excellent porosity, air permeability, and oxygen exchange, as well as desired mechanical strength and biodegradability. Particularly, the water uptake properties indicate their capacity to withhold moisture, which is essential for efficient diabetic wound healing applications. The fabricated PDGF/EuME–AgNPs exhibit greater antimicrobial efficacy against Gram-positive (*S. aureus*) and Gram-negative strains (*P. aeruginosa*). Furthermore, *in vivo* experiments confirm that PDGF/EuME–AgNPs/CSNs demonstrated a higher percentage of wound contraction and wound closure on the 9th day itself when compared to the control group and SBD–AgNPs/CSNs in the STZ-induced diabetic excisional wound rat models. In addition, histopathological studies (H&E staining and MT staining) reveal that the maximum amount of collagen deposition, fibroblast production, and fibrin regeneration is observed in wounds treated with PDGF/EuME–AgNPs/CSNs when compared to the control group and SBD–AgNPs/CSNs. Similarly, immunohistochemical studies prove that wounds treated with PDGF/EuME–AgNPs/CSNs showed increased production of CD-31, IL-1, and TGF-β, which confirmed re-epithelialization, vascularization, angiogenesis, expression of pro-inflammatory cytokines, and collagen deposition in the PDGF/EuME–AgNPs/CSNs-treated group. Therefore, based on the experimental results, it was confirmed that the fabricated PDGF/EuME–AgNPs/CSNs possess great potential as effective diabetic wound dressing scaffolds, which can further be taken for clinical trials and commercialization in the future, thereby suggesting their use in diabetic wound healing applications, and further molecular mechanistic insights are recommended in this direction.

## Conflicts of interest

All authors declare no professional or personal conflicts of interest.

## Data availability

The data supporting this article have been included as part of the supplementary information (SI). Supplementary information is available. See DOI: **https://doi.org/10.1039/d5ma00322a**.

## Acknowledgements

The authors are thankful to the Council of Scientific and Industrial Research, Government of India (CSIR-SRF) (File No. 09/844(0099)/2020 EMR-1) for funding this work and VIT University for providing the lab facilities to carry out the research work.

## References

1 A. Bezerra, H. Fonseca, F. Rodrigues, C. Delerue-Matos, I. Gouvinhas and J. Garcia, *Appl. Sci.*, 2023, **13**, 12820.
2 S. Priya, M. Choudhari, Y. Tomar, V. M. Desai, S. Innani, S. K. Dubey and G. Singhvi, *Carbohydr. Polym.*, 2023, **327**, 121655.
3 O. Sedighi, B. Bednarke, H. Sherriff and A. L. Doiron, *ACS Omega*, 2024, **9**, 27853–27871.
4 S. Bahadur and S. Fatima, *Curr. Pharm. Biotechnol.*, 2024, **25**, 1818–1834.
5 H. Liu, R. Chen, P. Wang, J. Fu, Z. Tang, J. Xie, Y. Ning, J. Gao, Q. Zhong, X. Pan and D. Wang, *Carbohydr. Polym.*, 2023, **316**, 121050.
6 Z. Zhou, Y. Zhang, Y. Zeng, D. Yang, J. Mo, Z. Zheng, Y. Zhang, P. Xiao, X. Zhong and W. Yan, *ACS Nano*, 2024, **18**, 7688–7710.
7 J. A. Mullin, E. Rahmani, K. L. Kiick and M. O. Sullivan, *BioTM*, 2024, **9**, e10642.
8 Y. F. Shao, H. Wang, Y. Zhu, Y. Peng, F. Bai, J. Zhang and K. Q. Zhang, *ACS Appl. Mater. Interfaces*, 2024, **16**, 60977–60991.
9 C. Wu, Q. Yu, C. Huang, F. Li, L. Zhang and D. Zhu, *Acta Pharm. Sin. B*, 2024, **14**(12), 5161–5180.
10 Y. Wang, X. Lu, J. Lu, P. Hernigou and F. Jin, *Front. Bioeng. Biotechnol.*, 2024, **12**, 1366398.
11 J. S. Franklyne, A. Ebenazer, A. Mukherjee and N. Chandrasekaran, *J. Drug Delivery Technol.*, 2021, **61**, 102158.
12 L. Sethuram, J. Thomas, A. Mukherjee and N. Chandrasekaran, *Mater. Adv.*, 2021, **2**, 2971–2988.
13 S. Maleki, A. Shamloo and F. Kalantarnia, *Sci. Rep.*, 2022, **12**, 6179.
14 S. Sun, M. Hao, C. Ding, J. Zhang, Q. Ding, Y. Zhang, Y. Zhao and W. Liu, *Colloids Surf., B*, 2022, **217**, 112692.
15 N. Fereydouni, J. Movaffagh, N. Amiri, S. Darroudi, A. Gholoobi, A. Goodarzi, A. Hashemzadeh and M. Darroudi, *Sci. Rep.*, 2021, **11**, 1902.
16 A. Alsaed, F. I. Elshami, M. M. Ibrahim, H. Shereef, H. Mohany, R. van Eldik and S. Y. Shaban, *J. Drug Delivery Sci. Technol.*, 2024, **97**, 105826.
17 L. Mayer, L. M. Weskamm, A. Fathi, M. Kono, J. Heidepriem, V. Krähling, S. C. Mellinghoff, M. L. Ly, M. Friedrich, S. Hardtke and S. Borregaard, *NPJ Vaccines*, 2024, **9**, 20.
18 M. Kumar, O. Frid, A. Sol, A. Rouvinski and S. Karniely, *bioRxiv*, 2024, preprint, 07, DOI: **10.1101/2024.07.18.604162**.

19 A. Alexandrova-Watanabe, E. Abadjieva, L. Gartcheva, A. Langari, M. Ivanova, M. Guenova, T. Tiankov, V. Strijkova, S. Krumova and S. Todinova, *Micromachines*, 2025, **16**, 95.
20 Y. Zhao, M. Brandon-Coatham, M. Yazdanbakhsh, O. Mykhailova, N. William, R. Osmani, T. Kanias and J. P. Acker, *Sci. Rep.*, 2025, **15**, 7735.
21 J. Krauß, R. Georgieva, M. Karabaliev, M. Hackmann, P. Rerkshanandana, S. Chaiwaree, U. Kalus, A. Pruß, Y. Xiong and H. Bäumler, *Nanomater*, 2025, **15**, 187.
22 A. L. de Sousa, L. M. Rebouças, F. M. Lemos, A. C. Barbosa, F. E. Cunha, C. Pessoa, S. L. Sales, L. M. Silva and N. M. Ricardo, *J. Drug Delivery Technol.*, 2025, 106746.
23 K. Das, H. Xu, J. Gu, S. Sakurai, V. Tiwari, S. K. Banerjee and V. Katiyar, *J. Appl. Polym. Sci.*, 2025, **142**, e56759.
24 Z. Gu, Z. Lu, J. Y. Wu, Z. Xie, R. Hu, Q. Huang, F. Liu and B. Zhang, *Food Funct.*, 2025.
25 S. C. Ganguly, B. Mahanti, S. Ganguly and S. Majumdar, *Int. J. Biol. Macromol.*, 2024, **278**, 134651.
26 Y. H. Cheng, H. K. Li, C. A. Yao, J. Y. Huang, Y. T. Sung, S. D. Chung and C. T. Chien, *PLoS One*, 2022, **17**, e0275748.
27 O. E. Adeleye, J. M. Enikuomehin, E. S. Ajibola, O. A. Adekoya, A. I. Adeleye and C. O. Oguntoye, *Alex. J. Vet. Sci.*, 2022, **75**, 25–33.
28 A. A. M. Ali, E. A. R. Essawy, N. S. Mohamed, A. E. Abdel Moneim and F. A. Attaby, *ESPR*, 2022, **29**, 12300–12312.
29 D. Prema, P. Balashanmugam, J. S. Kumar and G. D. Venkatasubbu, *Colloids Surf., A*, 2022, **649**, 129331.
30 S. Preet, S. Sharma, A. Panjeta, J. Kaur, A. Alshammari, M. Alharbi and S. Almawash, *Int. J. Pept. Res. Ther.*, 2022, **28**, 147.
31 M. B. Madiwalar, R. R. Hiremath and R. S. Killedar, *J. Ayurveda Integr. Med.*, 2022, **13**, 100602.
32 C. M. Hsieh, T. L. Yang, A. D. Putri and C. T. Chen, *Pharm*, 2023, **16**, 283.
33 T. Suthar, T. Patel, P. Singh, A. K. Datusalia, A. K. Yadav and K. Jain, *J. Drug Delivery Sci. Technol.*, 2023, **80**, 104166.
34 S. Jacob, F. S. Kather, S. H. Boddu, J. Shah and A. B. Nair, *Pharm*, 2024, **16**, 1333.
35 I. B. Basumatary, A. Mukherjee, V. Katiyar, J. Dutta and S. Kumar, *LWT*, 2022, **168**, 113940.
36 E. Stoleru, R. P. Dumitriu, G. L. Ailiesei, C. Yilmaz and M. Brebu, *Gels*, 2022, **8**, 225.
37 S. I. Sadia, M. K. H. Shishir, S. Ahmed, M. A. Alam, S. M. Al-Reza, S. Afrin, A. A. Pappu and S. A. Jahan, *NANO*, 2024, **39**, 101272.
38 M. Mehran, S. Masoum and M. Memarzadeh, *J. Dispersion Sci. Technol.*, 2024, **46**(1), 108–118.
39 A. R. Gliga, S. Skoglund, I. Odnevall Wallinder, B. Fadeel and H. L. Karlsson, *Part. Fibre Toxicol.*, 2014, **11**(1), 11.
40 V. Tekin, O. Kozgus Guldu, E. Dervis, A. Yurt Kilcar, E. Uygur and F. Z. Biber Muftuler, *Appl. Organomet. Chem.*, 2019, **33**, e4969.
41 K. Vijayaraghavan, S. K. Nalini, N. U. Prakash and D. J. M. L. Madhankumar, *Mater. Lett.*, 2012, **75**, 33–35.
42 F. Mokhtari, A. Samadi, A. O. Rashed, X. Li, J. M. Razal, L. Kong, R. J. Varley and S. Zhao, *Prog. Mater. Sci.*, 2025, **148**, 101376.
43 A. M. Yessuf, M. Bahri, T. S. Kassa, B. P. Sharma, A. M. Salama, C. Xing, Q. Zhang and Y. Liu, *ACS Appl. Bio Mater.*, 2024, **7**, 4231–4253.
44 G. C. Türkoğlu, N. Khomarloo, E. Mohsenzadeh, D. N. Gospodinova, M. Neznakomova and F. Salaün, *Int. J. Mol. Sci.*, 2024, **25**(3), 1668.
45 D. Tripathi, P. S. Rajinikanth and P. Pandey, *J. Mater. Chem. B*, 2025, **13**, 10743–10779.
46 S. Parham, A. Z. Kharazi, H. R. Bakhsheshi-Rad, H. Ghayour, A. F. Ismail, H. Nur and F. Berto, *Mater*, 2020, **13**(9), 2153.
47 H. Lv, S. Cui, Q. Yang, X. Song, D. Wang, J. Hu, Y. Zhou and Y. Liu, *Mater. Sci. Eng., C*, 2021, **118**, 111331.
48 Q. Asgari, M. Alishahi, F. Davani, D. Caravan, M. Khorram, Y. Enjavi, S. Barzegar, F. Esfandiari and K. Zomorodian, *Int. J. Pharm.*, 2021, **606**, 120911.
49 M. Rezaei, S. A. Hashemifard and M. Abbasi, *J. Appl. Polym. Sci.*, 2022, **139**, e52719.
50 G. C. Türkoğlu, N. Khomarloo, E. Mohsenzadeh, D. N. Gospodinova, M. Neznakomova and F. Salaün, *Int. J. Mol. Sci.*, 2024, **25**, 1668.
51 K. T. Chaka, K. Cao, T. Tesfaye and X. Qin, *J. Biomater. Sci., Polym. Ed.*, 2025, **36**, 371–413.
52 X. Hu, X. Chen, M. Giagnorio, C. Wu, Y. Luo, C. Hélix-Nielsen, P. Yu and W. Zhang, *J. Membr. Sci.*, 2022, **661**, 120850.
53 X. Ren, Y. Hu, L. Chang, S. Xu, X. Mei and Z. Chen, *Regen. Biomater.*, 2022, **9**, rbac012.
54 S. Ashtiani, T. Přibyl, J. Schneider, M. Khoshnamvand, F. Průša, T. Ruml, J. Floreková, D. Gardenö, J. Zelenka, Z. Sofer and K. Friess, *Environ. Res.*, 2025, **274**, 121234.
55 S. Sen, T. Bal and A. D. Rajora, *Appl. Nanosci.*, 2022, **12**, 237–250.
56 N. A. Ibrahim, S. Bibi, A. K. Khan and G. Murtaza, *J. Exp. Nanosci.*, 2022, **17**, 34–46.
57 R. Varma and S. Vasudevan, *ACS Omega*, 2020, **5**, 20224–20230.
58 E. A. El-Hefian, M. M. Nasef and A. H. Yahaya, *J. Chem.*, 2010, **7**, 1212–1219.
59 F. da Silva Bruckmann, A. R. Viana, L. Q. S. Lopes, R. C. V. Santos, E. I. Muller, S. R. Mortari and C. R. B. Rhoden, *J. Inorg. Organomet. Polym. Mater*, 2022, **32**, 1459–1472.
60 K. Pramod, C. V. Suneesh, S. Shanavas, S. H. Ansari and J. Ali, *J. Anal. Sci. Technol.*, 2015, **6**, 1–14.
61 K. H. Bodek, K. M. Nowak, M. Kozakiewicz, A. Bodek and M. Michalska, *Int. J. Polym. Sci.*, 2015, 386251.
62 A. R. Aidid, M. K. H. Shishir, M. A. Rahaman, M. T. Islam, M. Mukta and M. A. Alam, *Next Mater.*, 2025, **8**, 100571.
63 E. M. Abdel Bary, Y. A. Soliman, A. Fekri and A. N. Harmal, *Int. J. Environ. Stud.*, 2018, **75**, 750–762.
64 S. Wu, K. Li, W. Shi and J. Cai, *Int. J. Biol. Macromol.*, 2022, **210**, 76–84.
65 M. Anraku, Y. Mizukai, Y. Maezaki, K. Kawano, S. Okazaki, K. Takeshita, T. Adachi, M. Otagiri, D. Iohara and F. Hirayama, *Carbohydr. Polym.*, 2021, **253**, 117246.
66 C. Güneş Çimen, M. A. Dündar, M. Demirel Kars and A. Avcı, *ACS Biomater. Sci. Eng.*, 2022, **8**, 3717–3732.

67 H. Gao, H. Yang and C. Wang, *Results Phys.*, 2017, **7**, 3130–3136.
68 J. Lee, S. J. Huh, J. M. Seok, S. Lee, H. Byun, G. N. Jang, E. Kim, S. J. Kim, S. A. Park, S. M. Kim and H. Shin, *Acta Biomater.*, 2022, **140**, 730–744.
69 H. M. ohit, S. M. Rangappa, F. Gapsari, S. Siengchin, H. M. Marwani, A. Khan and A. M. Asiri, *J. Mater. Res. Technol.*, 2023, **23**, 5440–5458.
70 L. Lou, W. Yu, R. J. Kendall, E. Smith and S. S. Ramkumar, *J. Appl. Polym. Sci.*, 2020, **137**, 49213.
71 M. Koosha and H. Mirzadeh, *J. Biomed. Mater. Res. A*, 2015, **103**, 3081–3093.
72 N. T. Ardekani, M. Khorram, K. Zomorodian, S. Yazdanpanah, H. Veisi and H. Veisi, *Int. J. Biol. Macromol.*, 2019, **125**, 743–750.
73 A. Asiri, S. Saidin, M. H. Sani and R. H. Al-Ashwal, *Sci. Rep.*, 2021, **11**, 5634.
74 T. Dong, C. Han, X. Liu, Z. Wang, Y. Wang, Q. Kang, P. Wang and F. Zhou, *Mol. Pharmaceutics*, 2023, **20**, 2094–2104.
75 F. Madani, B. Mujokoro, S. Mohammadi, M. Khosravani and M. Adabi, *Nanomed. Res. J.*, 2022, **7**, 150–155.
76 C. Wang and M. Wang, *J. Mater. Sci.: Mater. Med.*, 2012, **23**, 2381–2397.
77 A. Ali, M. A. Shahid, M. D. Hossain and M. N. Islam, *Int. J. Biol. Macromol.*, 2019, **138**, 13–20.
78 M. Parani, G. Lokhande, A. Singh and A. K. Gaharwar, *ACS Appl. Mater. Interfaces*, 2016, **8**, 10049–10069.
79 A. Jahani, M. S. Nourbakhsh, A. Moradi, M. Mohammadi and L. Tayebi, *Carbohydr. Polym. Technol. Appl.*, 2025, 100696.
80 K. Lee and S. Lee, *Fiber Polym.*, 2020, **21**, 999–1012.
81 N. R. Vendidandala, T. P. Yin, G. Nelli, V. R. Pasupuleti, S. Nyamathulla and S. I. Mokhtar, *Life Sci.*, 2021, **286**, 120019.
82 H. P. Nagaiah, M. B. Samsudeen, A. R. Augustus and K. P. Shunmugiah, *Discov. Nano*, 2025, **20**, 14.
83 W. Wang, J. Ye, Z. Guo, Y. Ma, Q. Yang, W. Zhong, S. Du and J. Bai, *Int. J. Biol. Macromol.*, 2023, **239**, 124267.
84 Y. Dutt, R. P. Pandey, M. Dutt, A. Gupta, A. Vibhuti, V. S. Raj and C. M. Chang, *J. Biomed. Nanotechnol.*, 2022, **18**, 2022–2057.
85 M. S. Hassani, M. Salehi, A. Ehterami, S. Mahami, F. S. Bitaraf and M. Rahmati, *Biochem. Eng. J.*, 2023, **195**, 108895.
86 S. A. El-Zahaby, M. M. Wen, I. A. Abdelwahab, Y. M. Shahine, Y. M. Abdelhady and G. A. Elbatouti, *AAPS PharmSciTech*, 2024, **26**, 15.
87 Y. Du, Z. Yang, S. Kang, D. G. Yu, X. Chen and J. Shao, *Sensors*, 2023, **23**, 3685.
88 A. Shariati, S. M. Hosseini, Z. Chegini, A. Seifalian and M. R. Arabestani, *Biomed. Pharmacother.*, 2023, **158**, 114184.
89 F. Mao, Y. Su, X. Sun, B. Li and P. F. Liu, *ACS Omega*, 2023, **8**, 2733–2739.
90 S. Y. Zheng, X. X. Wan, P. A. Kambey, Y. Luo, X. M. Hu, Y. F. Liu, J. Q. Shan, Y. W. Chen and K. Xiong, *World J. Diabetes*, 2023, **14**, 364.
91 L. R. L. Diniz, L. R. L. Calado, A. B. S. Duarte and D. P. de Sousa, *Metabolites*, 2023, **13**, 276.
92 L. Fang, X. Lin, R. Xu, L. Liu, Y. Zhang, F. Tian, J. J. Li and J. Xue, *Nanomicro Lett.*, 2025, **17**, 1–46.
93 Z. Gao, Q. Qi, R. Li, C. Li, X. Xie and G. Hou, *Colloids Surf., B*, 2023, **224**, 113209.
94 P. Phutane, D. Telange, S. Agrawal, M. Gunde, K. Kotkar and A. Pethe, *Polymers*, 2023, **15**, 1202.
95 M. Alizadeh, S. Salehi, M. Tavakoli, M. Mirhaj, J. Varshosaz, N. Kazemi, S. Salehi, M. Mehrjoo and S. A. M. Abadi, *Int. J. Biol. Macromol.*, 2023, **233**, 123491.
96 Y. Dutt, R. P. Pandey, M. Dutt, A. Gupta, A. Vibhuti, V. S. Raj, C. M. Chang and A. Priyadarshini, *Antibiotics*, 2023, **12**, 121.
97 G. Ajith, G. P. Tamilarasi, G. Sabarees, S. Gouthaman, K. Manikandan, V. Velmurugan, V. Alagarsamy and V. R. Solomon, *Drugs Drug Candidates*, 2023, **2**, 148–171.
98 I. H. Ali, I. A. Khalil and I. M. El-Sherbiny, *Sci. Rep.*, 2023, **13**, 3215.
99 Z. Chen, K. Chan, X. Li, L. Gong, Y. Ma, C. Huang, Y. Lu, L. Wang and C. Piao, *Int. J. Nanomed.*, 2025, 6423–6446.
100 M. Winter, B. Heitplatz, N. Koppers, A. Mohr, A. D. Bungert, M. A. Juratli, B. Strücker, G. Varga, A. Pascher and F. Becker, *Cells*, 2023, **12**, 1039.
101 M. A. Islam, M. A. Haque, M. A. Rahman, F. Hossen, M. Reza, A. Barua, A. A. Marzan, T. Das, S. Kumar Baral, C. He and C. Ahmed, *Front. Immunol*, 2022, **13**, 837290.
102 A. Kalonia, A. K. Sharma, P. Shaw, A. Kumar, A. N. Bhatt, A. Shukla and S. K. Shukla, *Cytokine*, 2023, **164**, 156158.